PTEP

Prog. Theor. Exp. Phys. **2012**, 01A107 (36 pages)
DOI: 10.1093/ptep/pts030

Quantum electrodynamics calculation of lepton anomalous magnetic moments: Numerical approach to the perturbation theory of QED

Tatsumi Aoyama[1,2], Masashi Hayakawa[3,2], Toichiro Kinoshita[4,2], and Makiko Nio[2]

[1]*Kobayashi-Maskawa Institute for the Origin of Particles and the Universe (KMI), Nagoya University, Nagoya 464-8602, Japan*
[2]*Nishina Center, RIKEN, Wako, Saitama 351-0198, Japan*
[3]*Department of Physics, Nagoya University, Nagoya 464-8602, Japan*
[4]*Laboratory for Elementary-Particle Physics, Cornell University, Ithaca, NY 14853, USA*

Received May 27, 2012; Revised July 31, 2012; Accepted August 1, 2012; Published November 05, 2012

In this review, we summarize the results of our numerical work carried out over nearly ten years on the complete determination of the 10th-order contribution to the anomalous magnetic moments of leptons in the perturbation theory of quantum electrodynamics. Our approach is based on a reorganized renormalization method in which no divergent quantities appear explicitly in any part of the calculation, which is crucial for the feasibility of numerical integration. The enormous number of 10th-order diagrams and the complexity of the renormalization procedure are such that we could not have handled this problem without the development of an automated code-generating algorithm. The systematic approach to these problems is described in some detail.

1. Introduction

The anomalous magnetic moment of the electron a_e was discovered in 1947 by Kusch and Foley [1–3]. They measured the Zeeman splitting of the gallium atom and found a few % deviation from Dirac's relativistic quantum mechanics. They inferred that this deviation results from the electron g value being slightly larger than Dirac's prediction $g = 2$:

$$a_e = (g_e - 2)/2 = 0.001\,15\,(4). \tag{1.1}$$

Together with the discovery of the Lamb shift [4], this gave a timely stimulus to the renormalization theory of quantum electrodynamics (QED), which was being developed by Tomonaga [5,6] and Schwinger [7]. Schwinger was the first to calculate a_e in the framework of QED [8]. His result

$$a_e = \frac{\alpha}{2\pi} = 0.001\,161\cdots, \tag{1.2}$$

where α is the fine structure constant, was in good agreement with the experiment, providing a convincing proof of the validity of the newly developed QED.

Over the sixty years since 1947, many physicists have been involved in precision tests of the electron and muon anomalous magnetic moments. The history of the physics of lepton $g - 2$, both experimental and theoretical, can be found, for instance, in a recent publication [9].

The latest electron $g - 2$ measurement by the Harvard Group was carried out using a cylindrical Penning trap [10–12]. Their initial result was announced in 2006 and the improved result was reported

in 2008:

$$a_e(\mathrm{HV06}) = 1\,159\,652\,180.76\,(0.76) \times 10^{-12}, \tag{1.3}$$

$$a_e(\mathrm{HV08}) = 1\,159\,652\,180.73\,(0.28) \times 10^{-12} \quad [0.24\,\mathrm{ppb}]. \tag{1.4}$$

The latter is nearly 15 times more accurate than the previous best measurement by the Seattle group [13].

The measurement of the anomalous magnetic moment of the muon a_μ is constrained by the short lifetime (2.197×10^{-6} s) of the muon. Thus, instead of a tiny Penning trap, the spin precession in a large muon storage ring is used to measure a_μ. The best value obtained so far is from the experiment at Brookhaven. The average of the negative and positive muon measurements leads to the world's best value of a_μ [14,15]:

$$a_\mu(\mathrm{BNL04}) = 116\,592\,080\,(63) \times 10^{-11} \quad [0.5\,\mathrm{ppm}]. \tag{1.5}$$

Recently, the proton-to-muon magnetic moment ratio, which is used to determine the strength of the magnetic field applied to the storage ring, has changed slightly [16]. This causes a small shift in a_μ [17,18]:

$$a_\mu(\mathrm{BNL08}) = 116\,592\,089\,(63) \times 10^{-11} \quad [0.5\,\mathrm{ppm}]. \tag{1.6}$$

The Brookhaven experiment was shut down, but two new experiments are being prepared at Fermilab [19] and J-PARC [20,21]. Both aim to improve the relative precision to 0.1 ppm.

Up to which order of the QED perturbation theory do we need to meet the precision of the measurements (1.4) and (1.6)? For the electron, the very high precision of experiment (1.4) demands an explicit theoretical value of the 10th-order term since

$$\left(\frac{\alpha}{\pi}\right)^5 \sim 0.07 \times 10^{-12} \tag{1.7}$$

is not much smaller than the uncertainty of (1.4). The situation for the muon $g-2$, whose measurement uncertainty in (1.6) is about 9000 times larger than (1.7), looks quite different. However, a_μ has a huge numerical factor due to virtual electron loops, which depends logarithmically on the mass ratio m_μ/m_e. At 10th order, the effects of the light-by-light-scattering loop and two vacuum-polarization loops amount to a factor ~ 750:

$$\sim 750\left(\frac{\alpha}{\pi}\right)^5 \sim 5.3 \times 10^{-11}, \tag{1.8}$$

which, although still small compared with the measurement uncertainty, is no longer negligible, and will become relevant when the experiment improves by an order of magnitude.

The number of Feynman diagrams contributing to the lepton $g-2$ increases with the order of perturbation at a faster than exponential rate. For the second, fourth, and sixth orders, the numbers of diagrams are 1, 7, and, 72, respectively; see Figs. 1, 2, and 3. All diagrams up to the sixth order are known analytically. However, even for the sixth order, the analytic work was not easy. It took almost fifty years after Schwinger's second-order calculation before all 72 diagrams of the sixth order were evaluated analytically. The numbers of eighth- and 10th-order diagrams are 891 and 12 672, respectively; see Figs. 4 and 5. Although some diagrams with relatively simple structure have been evaluated analytically, it looks almost impossible to carry out a higher-order QED calculation by analytic means.

At present, the only practical way to tackle the higher-order QED terms is by numerical integration. In Sects. 2 and 3, we summarize the results of our work on the electron $g-2$ and muon

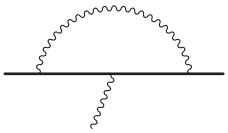

Fig. 1. Second-order diagram contributing to lepton $g-2$. There is one vertex Feynman diagram.

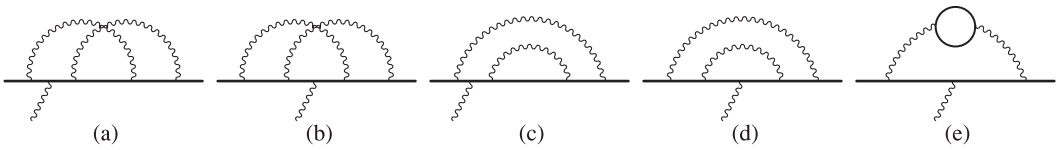

Fig. 2. Fourth-order diagrams contributing to lepton $g-2$. There are seven vertex Feynman diagrams, including the time-reversal symmetric diagrams.

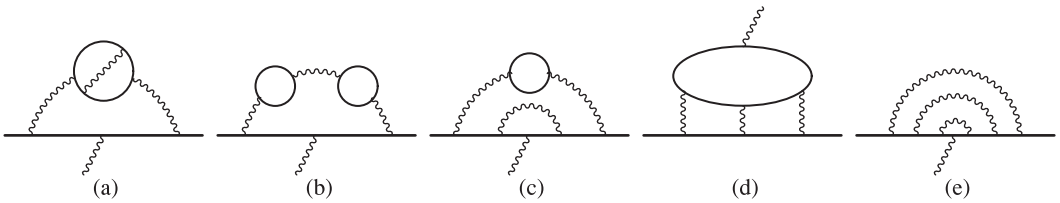

Fig. 3. Representative sixth-order vertex diagrams contributing to lepton $g-2$. There are 6 gauge-invariant groups consisting of 72 Feynman vertex diagrams.

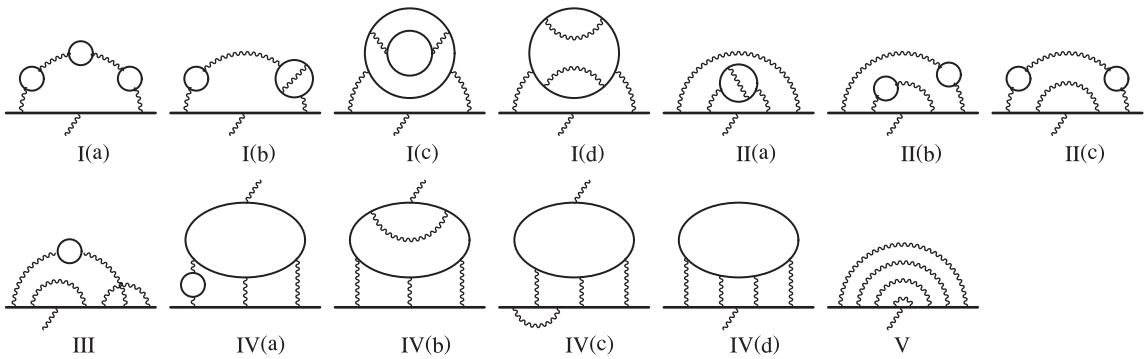

Fig. 4. Representative eighth-order vertex diagrams contributing to lepton $g-2$. There are 13 gauge-invariant groups consisting of 891 Feynman vertex diagrams.

$g-2$. Section 4 presents our formulation of the QED calculation, adapted to the requirement of numerical integration. Sections 5 and 6 are devoted to the treatment of ultraviolet (UV) and infrared (IR) divergences, respectively. The residual renormalization is explained in Sect. 7 by treating some lower-order diagrams as examples.

2. Theory of the electron $g-2$

Since the electron is the lightest of the leptons, it is little affected by much heavier particles, such as hadrons and weak bosons. In this sense the electron $g-2$ is almost a pure QED system. In order to compare the QED prediction of a_e to the measurement, we need three input values from outside of QED: the fine-structure constant α, the electron–muon mass ratio $m_e/m_\mu = 4.836\,331\,66\,(12) \times 10^{-3}$, and the electron–tau mass ratio $m_e/m_\tau = 2.875\,92\,(26) \times 10^{-4}$ [22]. Within the standard

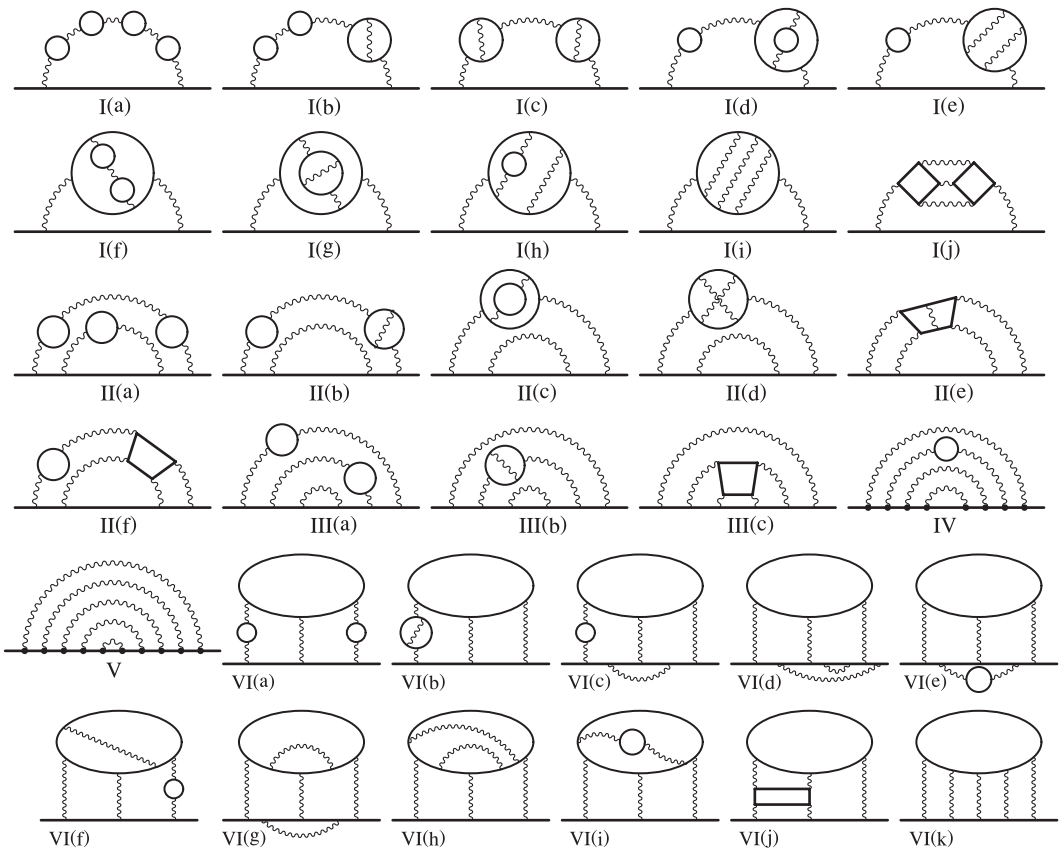

Fig. 5. Representative 10th-order self-energy-like diagrams. Vertex diagrams corresponding to the diagrams of types I to V are generated by inserting an external magnetic vertex in the open fermion lines in all possible ways. For the type VI diagrams, the external magnetic vertex must be inserted in the light-by-light-scattering loops. This gives rise to 32 gauge-invariant sets consisting of 12 672 vertex diagrams that contribute to lepton $g-2$. Reproduced with permission from [48].

model of the elementary particles, a_e can be written as

$$a_e(\text{theory}) = a_e(\text{QED}) + a_e(\text{hadron}) + a_e(\text{weak}). \tag{2.1}$$

The renormalizability of the perturbation theory of QED guarantees that $a_e(\text{QED})$ is described as the power series of α

$$a_e(\text{QED}) = a_e^{(2)}\left(\frac{\alpha}{\pi}\right) + a_e^{(4)}\left(\frac{\alpha}{\pi}\right)^2 + a_e^{(6)}\left(\frac{\alpha}{\pi}\right)^3 + a_e^{(8)}\left(\frac{\alpha}{\pi}\right)^4 + \cdots . \tag{2.2}$$

The mass dependence of the coefficients of the perturbation series $a_e^{(2n)}, n = 1, 2, 3, \ldots$ can be expressed as

$$a_e^{(2n)} = A_1^{(2n)} + A_2^{(2n)}(m_e/m_\mu) + A_2^{(2n)}(m_e/m_\tau) + A_3^{(2n)}(m_e/m_\mu, m_e/m_\tau). \tag{2.3}$$

The second-, fourth-, and sixth-order contributions were obtained analytically or as power series expansion in m_e/m_μ or m_e/m_τ [7,23–30]. They are consistent with numerical calculations [31]:

$$A_1^{(2)} = 0.5 \tag{2.4}$$

$$A_1^{(4)} = \frac{197}{144} + \frac{\pi^2}{12} + \frac{3}{4}\zeta(3) - \frac{\pi^2}{2}\ln 2 = -0.328\,478\,965\,579\,193\cdots \tag{2.5}$$

$$A_2^{(4)}(m_e/m_\mu) = 5.197\,386\,67\,(26) \times 10^{-7}, \tag{2.6}$$

$$A_2^{(4)}(m_e/m_\tau) = 1.837\,98\,(34) \times 10^{-9}, \tag{2.7}$$

$$\begin{aligned} A_1^{(6)} &= \frac{83}{72}\pi^2\zeta(3) - \frac{215}{24}\zeta(5) - \frac{239}{2160}\pi^4 + \frac{139}{18}\zeta(3) - \frac{298}{9}\pi^2\ln 2 \\ &\quad + \frac{17\,101}{810}\pi^2 + \frac{28\,259}{5184} + \frac{100}{3}\left\{a_4 + \frac{1}{24}(\ln^2 2 - \pi^2)\ln^2 2\right\} \\ &= 1.181\,241\,456\cdots, \end{aligned} \tag{2.8}$$

$$A_2^{(6)}(m_e/m_\mu) = -7.373\,941\,55\,(27) \times 10^{-6}, \tag{2.9}$$

$$A_2^{(6)}(m_e/m_\tau) = -6.5830\,(11) \times 10^{-8}, \tag{2.10}$$

$$A_3^{(6)}(m_e/m_\mu, m_e/m_\tau) = 1.909\,(1) \times 10^{-13}, \tag{2.11}$$

where $\zeta(s)$ is the Riemann zeta function of argument s and

$$a_4 = \sum_{n=1}^{\infty} \frac{1}{2^n n^4} = 0.517\,479\,061\cdots. \tag{2.12}$$

The uncertainties come only from the measurement of the lepton mass ratios. There are no three-lepton-mass-dependent contributions at the second and fourth orders, namely, $A_3^{(2)}(m_e/m_\mu, m_e/m_\tau) = A_3^{(4)}(m_e/m_\mu, m_e/m_\tau) = 0$. The sixth-order three-lepton-mass-dependent term $A_3^{(6)}(m_e/m_\mu, m_e/m_\tau)$ gives a contribution of $\mathcal{O}(10^{-21})$ to a_e, and is completely negligible compared with the current experimental precision 0.28×10^{-12}.

The eighth- and 10th-order contributions have been obtained mostly by numerical means (T. Aoyama et al., manuscript in preparation, and Refs. [32–48]), except for a few simple diagrams that were evaluated analytically [49,50]. Our recent numerical evaluation of all eighth- and 10th-order contributions is summarized as follows [48]:

$$A_1^{(8)} = -1.9106\,(20), \tag{2.13}$$

$$A_2^{(8)}(m_e/m_\mu) = 9.222\,(66) \times 10^{-4}, \tag{2.14}$$

$$A_2^{(8)}(m_e/m_\tau) = 8.24\,(12) \times 10^{-6}, \tag{2.15}$$

$$A_3^{(8)}(m_e/m_\mu, m_e/m_\tau) = 7.465\,(18) \times 10^{-7}, \tag{2.16}$$

$$A_1^{(10)} = 9.16\,(58), \tag{2.17}$$

$$A_2^{(10)}(m_e/m_\mu) = -0.003\,82\,(39), \tag{2.18}$$

where the uncertainties are only those estimated by the numerical integration routine VEGAS [93].

Table 1. The eighth-order QED contribution from 13 gauge-invariant groups to electron $g-2$. n_f shows the number of vertex diagrams that belong to a gauge-invariant group contributing to $A_1^{(8)}$. The values with a superscript a, b, or c are quoted from Refs. [49], [33], or [32], respectively. Other values are obtained from evaluation of new programs. The mass dependence of $A_3^{(8)}$ is $A_3^{(8)}(m_e/m_\mu, m_e/m_\tau)$.

Group	n_f	$A_1^{(8)}$	$A_2^{(8)}(m_e/m_\mu)\times 10^3$	$A_2^{(8)}(m_e/m_\tau)\times 10^5$	$A_3^{(8)}\times 10^7$
I(a)	1	0.000 876 865 $\cdots$[a]	0.000 226 456 (14)	0.000 080 233 (5)	0.000 011 994 (1)
I(b)	6	0.015 325 20 (37)	0.001 704 139 (76)	0.000 602 805 (26)	0.000 014 097 (1)
I(c)	3	0.011 130 8 (9)[b]	0.011 007 2 (15)	0.006 981 9 (12)	0.172 860 (21)
I(d)	15	0.049 514 8 (38)	0.002 472 5 (7)	0.087 44 (1)	0
II(a)	36	−0.420 476 (11)	−0.086 446 (9)	−0.045 648 (7)	0
II(b)	6	−0.027 674 89 (74)	−0.039 000 3 (27)	−0.030 393 7 (42)	−0.458 968 (17)
II(c)	12	−0.073 445 8 (54)	−0.095 097 (24)	−0.071 697 (25)	−1.189 69 (67)
III	150	1.417 637 (67)	0.817 92 (95)	0.6061 (12)	0
IV(a)	18	0.598 838 (19)	0.635 83 (44)	0.451 17 (69)	8.941 (17)
IV(b)	60	0.822 36 (13)	0.041 05 (93)	0.014 31 (95)	0
IV(c)	48	−1.138 52 (20)	−0.1897 (64)	−0.102 (11)	0
IV(d)	18	−0.990 72 (10)[c]	−0.1778 (12)	−0.0927 (13)	0
V	518	−2.1755 (20)	0	0	0

The previously published value of $A_1^{(8)}$ is [33,37,38]

$$A_1^{(8)}[2007] = -1.9144\,(35). \tag{2.19}$$

As described in Refs. [35] and [36], we have automated computer programming of the $g-2$ calculation for diagrams without a fermion loop. This system is called gencode*N*. In Refs. [37] and [38], the eighth-order contribution from the diagrams without a fermion loop, called Group V (the last diagram of Fig. 4), was reevaluated using the fortran codes generated by gencode*N*. After numerical evaluation carried out over nearly two years, we obtained

$$A_1^{(8)}[\text{Group V 2012}] = -2.173\,56\,(235), \tag{2.20}$$

which is consistent with the earlier result [37,38]

$$A_1^{(8)}[\text{Group V 2007}] = -2.179\,16\,(343). \tag{2.21}$$

Since these two results are obtained by completely different programs derived from different algorithms, they are independent of each other. Therefore, we combined them statistically, obtaining

$$A_1^{(8)}[\text{Group V}] = -2.175\,50\,(194). \tag{2.22}$$

The eighth-order contributions from other diagrams are also slightly improved by intensive numerical work. The value of $A_1^{(8)}$ in (2.13) takes account of all these improvements. The numerical values of each gauge-invariant group are shown in Table 1.

The 10th-order mass-independent term $A_1^{(10)}$ receives a contribution from the 12 672 diagrams shown in Fig. 5. We started the project to evaluate all 10th-order diagrams nearly ten years ago. Thus far, the results of 31 gauge-invariant sets have been published [34,39–47]. The results for the remaining set will be reported shortly (T. Aoyama et al., manuscript in preparation). The value (2.17) is the preliminary result of our evaluation [48]. The contributions from all 32 gauge-invariant sets are shown in Table 2.

Table 2. Summary of contributions to the 10th-order lepton $g-2$ from 32 gauge-invariant subsets. n_F is the number of vertex diagrams contributing to $A_1^{(10)}$. The numerical values of individual subsets were originally obtained in the references in the fifth column. The values $A_1^{(10)}$ of subsets I(d), I(f), II(a), II(b), and VI(c) in Ref. [34] are corrected in Ref. [48].

Set	n_F	$A_1^{(10)}$	$A_2^{(10)}(m_e/m_\mu)$	Reference
I(a)	1	0.000 470 94 (6)	0.000 000 28 (1)	[34]
I(b)	9	0.007 010 8 (7)	0.000 001 88 (1)	[34]
I(c)	9	0.023 468 (2)	0.000 002 67 (1)	[34]
I(d)	6	0.003 801 7 (5)	0.000 005 46 (1)	[34],[48]
I(e)	30	0.010 296 (4)	0.000 001 60 (1)	[34]
I(f)	3	0.007 568 4 (20)	0.000 047 54 (1)	[34],[48]
I(g)	9	0.028 569 (6)	0.000 024 45 (1)	[40]
I(h)	30	0.001 696 (13)	−0.000 010 14 (3)	[40]
I(i)	105	0.017 47 (11)	0.000 001 67 (2)	[44]
I(j)	6	0.000 397 5 (18)	0.000 002 41 (6)	[39]
II(a)	24	−0.109 495 (23)	−0.000 737 69 (95)	[34],[48]
II(b)	108	−0.473 559 (84)	−0.000 645 62 (95)	[34],[48]
II(c)	36	−0.116 489 (32)	−0.000 380 25 (46)	[43]
II(d)	180	−0.243 00 (29)	−0.000 098 17 (41)	[43]
II(e)	180	−1.344 9 (10)	−0.000 465 0 (40)	[41]
II(f)	72	−2.433 6 (15)	−0.005 868 (39)	[34]
III(a)	300	2.127 33 (17)	0.007 511 (11)	[45]
III(b)	450	3.327 12 (45)	0.002 794 (1)	[45]
III(c)	390	4.921 (11)	0.003 70 (36)	[47]
IV	2072	−7.7296 (48)	−0.011 36 (7)	[46]
V	6354	10.09 (57)	0	[48]
VI(a)	36	1.041 32 (19)	0.006 152 (11)	[34]
VI(b)	54	1.346 99 (28)	0.001 778 9 (35)	[34]
VI(c)	144	−2.5289 (28)	−0.005 953 (59)	[34],[48]
VI(d)	492	1.8467 (70)	0.001 276 (76)	[42]
VI(e)	48	−0.4312 (7)	−0.000 750 (8)	[34]
VI(f)	180	0.7703 (22)	0.000 033 (7)	[34]
VI(g)	480	−1.5904 (63)	−0.000 497 (29)	[42]
VI(h)	630	0.1792 (39)	0.000 045 (9)	[42]
VI(i)	60	−0.0438 (12)	−0.000 326 (1)	[34]
VI(j)	54	−0.2288 (18)	−0.000 127 (13)	[34]
VI(k)	120	0.6802 (38)	0.000 015 6 (40)	[34]

Until the value (2.17) becomes available, the educated-guess value proposed in Ref. [51],

$$A_1^{(10)} = 0.0\,(4.6), \tag{2.23}$$

was widely used. Its uncertainty, 4.6, was obtained by extrapolating the absolute values of the mass-independent results $A_1^{(6)}$ and $A_1^{(8)}$ of (2.8) and (2.19), respectively, to the 10th order.

The muon loop effect (2.18) of the 10th-order term $A_2^{(10)}(m_e/m_\mu)$ gives a contribution of $\mathcal{O}(10^{-16})$ to a_e and is negligible compared with the experimental precision. The tau-lepton loop effect at the 10th order is estimated to be at least a factor of 10 smaller than the muon loop effect. Thus, we currently ignore $A_2^{(10)}(m_e/m_\tau)$ and $A_3^{(10)}(m_e/m_\mu, m_e/m_\tau)$.

In view of the precision of the Harvard experiment (1.4), the hadronic and weak contributions to the electron $g-2$ are no longer negligible. The hadronic vacuum-polarization (had. v.p.) effect has been calculated as [52]

$$a_e(\text{had. v.p.}) = 1.866(12) \times 10^{-12} - 0.2234(14) \times 10^{-12}, \tag{2.24}$$

where the first and second terms are the leading-order and next-to-leading-order contributions from the hadronic vacuum-polarization, respectively. The values in (2.24) are consistent with those

obtained from the vaccum-polarization contribution to the muon $g-2$ [53–55], multiplying the factor $(m_e/m_\mu)^2$.

The contribution from hadronic light-by-light (had. *l-l*) scattering has been calculated for the electron $g-2$ [56]

$$a_e(\text{had. } l\text{-}l) = 0.035\,(10) \times 10^{-12}. \tag{2.25}$$

The weak contribution is also calculated for the muon $g-2$ and its effect on the electron $g-2$ is obtained by scaling it down to the electron [57–60]:

$$a_e(\text{weak}) = 0.0297\,(5) \times 10^{-12}. \tag{2.26}$$

In order to determine the theoretical prediction of a_e, we need the value of the fine-structure constant α, which cannot be determined by QED theory itself. One of the best values of α became available at the beginning of the year 2011 from the atom beam experiment. The precise value of the ratio between the Planck constant and the mass of the Rb atom (h/m_{Rb}) was obtained by using the optical lattice technique [61]. Together with the precisely known Rydberg constant R_∞ and the electron–Rb mass ratio m_e/m_{Rb}, the inverse of the fine-structure constant is obtained as [22]

$$\alpha^{-1}(\text{Rb}) = 137.035\,999\,049\,(90). \tag{2.27}$$

Substituting $\alpha^{-1}(\text{Rb})$ of (2.27) into the perturbation series (2.2) together with the hadronic and weak corrections, we obtain the theoretical prediction of a_e

$$a_e(\text{theory}) = 1\,159\,652\,181.78\,(0.06)(0.04)(0.02)(0.77)[0.77] \times 10^{-12}, \tag{2.28}$$

where the uncertainties from left to right are due to the numerical calculation (2.13) of the eighth-order term $A_1^{(8)}$, (2.17) of the 10th-order term $A_1^{(10)}$, the hadronic and electroweak corrections, and the fine-structure constant $\alpha^{-1}(\text{Rb})$. The last value within the brackets is their statistical combination. The uncertainty due to the fermion mass ratio is $\mathcal{O}(10^{-16})$. The agreement between the theory (2.28) and the experiment (1.4) is satisfactory:

$$a_e(\text{HV08}) - a_e(\text{theory}) = (-1.05 \pm 0.82) \times 10^{-12}. \tag{2.29}$$

As seen from (2.28), the uncertainty due to the fine-structure constant $\alpha^{-1}(\text{Rb})$ in (2.27) dominates over those due to other sources. This implies that we can obtain a value of the fine-structure constant better than the Rb-atom measurement assuming that the QED theory is valid. Equating the theory (2.1) and the measured value (1.4) and solving for the fine-structure constant, we obtain

$$\alpha^{-1}(a_e) = 137.035\,999\,1727\,(68)(46)(19)(331)[342], \tag{2.30}$$

where the uncertainties are due to the eighth-order term (2.13), the 10th-order term (2.17), the hadronic correction, the experiment (1.4), and their combination. The difference between the values of α^{-1} of (2.27) and (2.30) is

$$\alpha^{-1}(\text{Rb}) - \alpha^{-1}(a_e) = (-124 \pm 97) \times 10^{-9}. \tag{2.31}$$

It is interesting to see what will happen to the difference when the precision of both α values is further improved.

3. Theory of the muon $g-2$

The anomalous magnetic moment is a dimensionless constant. Thus the mass-independent terms $A_1^{(2n)}$, $n = 1, 2, \ldots$ are common for all species of leptons. The term that makes a_μ distinguishable from a_e is the mass-dependent term, particularly the electron-loop contribution to a_μ that gives rise to the logarithmic enhancement factor $\ln(m_\mu/m_e)$. There are two sources of $\ln(m_\mu/m_e)$. One is the threshold singularity of vacuum-polarization diagrams. This term can be analytically traced using the renormalization group technique [62–68]. Another source is a diagram involving a light-by-light (*l*-*l*) scattering loop attached to the external magnetic field. This diagram first appears in the sixth-order perturbation theory. The early work on this *l*-*l* diagram by numerical means revealed that the *l*-*l* diagram produces the logarithmic factor $\ln(m_\mu/m_e)$ [69,70]. The mechanism of the origin of this logarithm was later clarified by the observation that the electron in the *l*-*l* loop and the external muon nearly form a Coulombic bound state [71,72].

The contributions up to the sixth order have been obtained analytically and double-checked by numerical calculations. The uncertainties of these terms are due to the measurement of the mass ratio of leptons only:

$$A_2^{(4)}(m_\mu/m_e) = 1.094\,258\,312\,0\,(83), \tag{3.1}$$

$$A_2^{(4)}(m_\mu/m_\tau) = 0.780\,79\,(15) \times 10^{-4}, \tag{3.2}$$

$$A_2^{(6)}(m_\mu/m_e) = 22.868\,380\,04\,(23), \tag{3.3}$$

$$A_2^{(6)}(m_\mu/m_\tau) = 0.360\,70\,(13) \times 10^{-3}, \tag{3.4}$$

$$A_3^{(6)}(m_\mu/m_e, m_\mu/m_\tau) = 0.527\,76\,(11) \times 10^{-3}, \tag{3.5}$$

where A_2 and A_3 of fourth and sixth order have been evaluated by numerical integration, analytic integration, asymptotic expansion in m_μ/m_e, or power series expansion in m_μ/m_τ [28–30,73–75]. Note that $A_3^{(4)} = 0$.

Recent evaluation of the eighth- and 10th-order contributions gives [76,77]

$$A_2^{(8)}(m_\mu/m_e) = 132.6852\,(60), \tag{3.6}$$

$$A_2^{(8)}(m_\mu/m_\tau) = 0.042\,34\,(12), \tag{3.7}$$

$$A_3^{(8)}(m_\mu/m_e, m_\mu/m_\tau) = 0.062\,715\,(36), \tag{3.8}$$

$$A_2^{(10)}(m_\mu/m_e) = 742.18\,(87), \tag{3.9}$$

$$A_2^{(10)}(m_\mu/m_\tau) = -0.0681\,(52), \tag{3.10}$$

$$A_3^{(10)}(m_\mu/m_e, m_\mu/m_\tau) = 2.011\,(10). \tag{3.11}$$

The uncertainties of these terms are those generated by VEGAS. Some of the diagrams have been analytically evaluated [50,78,79] and they are consistent with the results obtained by numerical calculations. The numerical values of individual eighth- and 10th-order gauge-invariant groups are shown in Table 3 and Table 4, respectively.

The previously published values [76] of $A_2^{(8)}(m_\mu/m_e)$ and $A_3^{(8)}(m_\mu/m_e, m_\mu/m_\tau)$ are

$$A_2^{(8)}(m_\mu/m_e)[2006] = 132.6823(72), \tag{3.12}$$

$$A_3^{(8)}(m_\mu/m_e, m_\mu/m_\tau)[2006] = 0.0376(1). \tag{3.13}$$

Table 3. The eighth-order mass-dependent QED contribution from 12 gauge-invariant groups to muon $g-2$, whose representatives are shown in Fig. 4. The mass dependence of $A_3^{(8)}$ is $A_3^{(8)}(m_\mu/m_e, m_\mu/m_\tau)$.

Group	$A_2^{(8)}(m_\mu/m_e)$	$A_2^{(8)}(m_\mu/m_\tau)$	$A_3^{(8)}$
I(a)	7.745 47 (42)	0.000 032 (0)	0.003 209 (0)
I(b)	7.582 01 (71)	0.000 252 (0)	0.002 611 (0)
I(c)	1.624 307 (40)	0.000 737 (0)	0.001 807 (0)
I(d)	−0.229 82 (37)	0.000 368 (0)	0.000 000 (0)
II(a)	−2.778 88 (38)	−0.007 329 (1)	0.000 000 (0)
II(b)	−4.552 77 (30)	−0.002 036 (0)	−0.009 008 (1)
II(c)	−9.341 80 (83)	−0.005 246 (1)	−0.019 642 (2)
III	10.7934 (27)	0.045 04 (14)	0
IV(a)	123.785 51 (44)	0.038 513 (11)	0.083 739 (36)
IV(b)	−0.4170 (37)	0.006 106 (31)	0
IV(c)	2.9072 (44)	−0.018 23 (11)	0
IV(d)	−4.432 43 (58)	−0.015 868 (37)	0

Table 4. Tenth-order mass-dependent contribution to the muon $g-2$ from 31 gauge-invariant subsets shown in Fig. 5. The mass dependence of $A_3^{(10)}$ is $A_3^{(10)}(m_\mu/m_e, m_\mu/m_\tau)$.

Set	$A_2^{(10)}(m_\mu/m_e)$	$A_2^{(10)}(m_\mu/m_\tau)$	$A_3^{(10)}$
I(a)	22.566 973 (3)	0.000 038 (0)	0.017 312 (1)
I(b)	30.667 091 (3)	0.000 269 (0)	0.020 179 (1)
I(c)	5.141 395 (1)	0.000 397 (0)	0.002 330 (0)
I(d)	8.8921 (11)	0.000 388 (0)	0.024 487 (2)
I(e)	−0.9312 (24)	0.000 232 (0)	0.002 370 (0)
I(f)	3.685 049 (90)	0.002 162 (0)	0.023 390 (2)
I(g)	2.607 87 (72)	0.001 698 (0)	0.002 729 (1)
I(h)	−0.5686 (11)	0.000 163 (1)	0.001 976 (3)
I(i)	0.0871 (59)	0.000 024 (0)	0
I(j)	−1.263 72 (14)	0.000 168 (1)	0.000 110 (5)
II(a)	−70.4717 (38)	−0.018 882 (8)	−0.290 853 (85)
II(b)	−34.7715 (26)	−0.035 615 (20)	−0.127 369 (60)
II(c)	−5.385 75 (99)	−0.016 348 (14)	−0.040 800 (51)
II(d)	0.4972 (65)	−0.007 673 (14)	0
II(e)	3.265 (12)	−0.038 06 (13)	0
II(f)	−77.465 (12)	−0.267 23 (73)	−0.502 95 (68)
III(a)	109.116 (33)	0.283 000 (32)	0.891 40 (44)
III(b)	11.9367 (45)	0.143 600 (10)	0
III(c)	7.37 (15)	0.1999 (28)	0
IV	−38.79 (17)	−0.4357 (25)	0
VI(a)	629.141 (12)	0.246 10 (18)	2.3590 (18)
VI(b)	181.1285 (51)	0.096 522 (93)	0.194 76 (26)
VI(c)	−36.58 (12)	−0.2601 (28)	−0.5018 (89)
VI(d)	−7.92 (60)	0.0818 (17)	0
VI(e)	−4.32 (14)	−0.035 94 (32)	−0.1122 (24)
VI(f)	−38.16 (15)	0.043 47 (85)	0.0659 (31)
VI(g)	6.96 (48)	−0.044 51 (96)	0
VI(h)	−8.55 (23)	0.004 85 (46)	0
VI(i)	−27.34 (12)	−0.003 45 (33)	−0.0027 (11)
VI(j)	−25.505 (20)	−0.011 49 (33)	−0.016 03 (58)
VI(k)	97.123 (62)	0.002 17 (16)	0

The new calculation of $A_2^{(8)}(m_\mu/m_e)$ using the automatically generated fortran codes is in good agreement with the result of the old calculation (3.12). Thus we combined the two results statistically and obtained the value given in (3.6). Unfortunately, the results (3.8) and (3.13) of the three-mass term $A_3^{(8)}(m_\mu/m_e, m_\mu/m_\tau)$ are very different from each other. We found that, in the old calculation (3.13), some of the integrals lack a symmetric factor 2 required to account for the exchange of the

electron loop and the tau-lepton loop. The value (3.13) is thus incorrect and must be replaced by (3.8). The contributions from individual gauge-invariant groups are shown in Table 3.

The 10th-order term $A_2^{(10)}(m_\mu/m_e)$ is the sum of the results of 31 of 32 gauge-invariant subsets shown in Fig. 5. The exception is Set V, which does not contribute to the mass-dependent term $A_2^{(10)}$. The mass-dependent contributions of individual subsets can be found in Refs. [34,39–47], and are summarized in Table 4.

Note that (3.9) is about 4 standard uncertainties larger than the previous estimate 663(20) [34]. This is mainly because we had underestimated the magnitude of the contribution of Set III(a).

Using the α^{-1}(Rb) of (2.27) and the latest values of the fermion mass ratios [22], we obtain the QED contribution to a_μ

$$a_\mu(\text{QED}) = 116\,584\,718.951\,(0.019)(0.007)(0.009)(0.077)\,[0.080] \times 10^{-11}, \tag{3.14}$$

where the uncertainties are due to the eighth-order term, the 10th-order term, the mass ratio m_τ/m_μ, α, and their statistical combination, respectively.

At present, a_μ(hadron) is the largest source of theoretical uncertainty. The uncertainty comes mostly from the hadronic vacuum-polarization term, which is calculable from the experimental information. Three types of measurements are available for this purpose:

1. $e^+e^- \to$ hadrons,
2. $e^+e^- \to \gamma +$ hadrons,
3. $\tau^\pm \to \nu + \pi^\pm + \pi_0$.

These processes have been closely investigated by many groups [53–55,80,81]. The ee-based analysis [53–55,81] uses both experiments 1 and 2, while the τ-based analysis [54,55] relies on experiment 3 only. The ee-based results obtained by several groups are consistent with each other. Meanwhile, the τ-based result was considerably different from the ee-based results. The recent τ-based result [54] is, however, very close to the ee-based results.

We list here one of those based on the ee analysis [53]:

$$a_\mu(\text{had. v.p.}) = 6949.1\,(37.2)_{\text{exp}}\,(21.0)_{\text{rad}} \times 10^{-11}. \tag{3.15}$$

The higher-order (ho) hadronic vacuum-polarization contribution is also known [53]:

$$a_\mu(\text{had. v.p. ho}) = -98.4(0.6)_{\text{exp}}(0.4)_{\text{rad}} \times 10^{-11}. \tag{3.16}$$

The hadronic light-by-light scattering contribution is a similar size to a_μ(had. v.p. ho), but has a much larger theoretical uncertainty [82–85]:

$$a_\mu(\text{had. } l\text{-}l) = 116\,(40) \times 10^{-11}. \tag{3.17}$$

The weak contribution has been calculated up to the 2-loop order [58–60]:

$$a_\mu(\text{weak}) = 154\,(2) \times 10^{-11}. \tag{3.18}$$

Since this uncertainty is 30 times smaller than the experimental precision of (1.6), it can be regarded as being known accurately.

Adding up all QED, hadronic, and weak contributions, the standard-model prediction of the muon $g-2$ is

$$a_\mu(\text{theory}) = 116\,591\,840\,(59)(2)\,[59] \times 10^{-11}, \tag{3.19}$$

where the uncertainties are, from left to right, from the hadronic and weak contributions, and a combination of the two. The uncertainty due to QED is negligible. The difference between the experiment

(1.6) and the theory (3.19) is

$$a_\mu(\text{BNL08}) - a_\mu(\text{theory}) = (249 \pm 87) \times 10^{-11}. \tag{3.20}$$

The difference is 2.9 times larger than the standard uncertainty.

4. Formulation of the a_e calculation

In this section, we give a general formalism to calculate the electron $g-2$ contribution in the QED perturbation theory. We work out the Feynman–Dyson rule directly in Feynman parametric space. The Feynman parametric integral formalism was first described in Ref. [86] and the details of it are also explained in Ref. [87]. This formalism is also used for our automation code gencode*N* [35]. We here quote the discussion from Ref. [35].

4.1. Definition of a_e amplitude

The magnetic property of a lepton can be studied through examining its scattering by a static magnetic field. The amplitude of this process including interactions with the virtual photon fields can be represented as follows, by taking account of the gauge symmetry, invariance under Lorentz, C, P, and T transformations:

$$e\bar{u}(p'')\left[\gamma^\mu F_1(q^2) + \frac{i}{2m}\sigma^{\mu\nu} q_\nu F_2(q^2)\right] u(p')\, A^e_\mu(\vec{q}), \tag{4.1}$$

where $p' = p - q/2$, $p'' = p + q/2$, $q = p'' - p'$ and $\sigma^{\mu\nu} = \frac{i}{2}(\gamma^\mu\gamma^\nu - \gamma^\nu\gamma^\mu)$. A^e_μ is the vector potential of the external static magnetic field. F_1 and F_2 are called the charge and magnetic form factors, respectively. The charge form factor is normalized so that $F_1(0) = 1$.

The anomalous magnetic moment a_e is the static limit of the magnetic form factor $F_2(q^2)$, and it is expressed as

$$a_e = F_2(0) = Z_2 M \tag{4.2}$$

with

$$M = \lim_{q^2\to 0} \text{Tr}(P_\nu(p,q)\,\Gamma^\nu), \tag{4.3}$$

where Z_2 is the wavefunction renormalization constant, Γ^ν is the proper vertex function with the external electrons on the mass shell, and $P_\nu(p,q)$ is the magnetic projection operator,

$$P^\nu(p,q) = \frac{1}{4(p^2)^2 q^2}\left(\not{p} - \frac{1}{2}\not{q} + m\right)\left[m\gamma^\nu p^2 - \left(m^2 + \frac{1}{2}q^2\right)p^\nu\right]\left(\not{p} + \frac{1}{2}\not{q} + m\right). \tag{4.4}$$

Here, the momentum of incoming lepton $p - \frac{1}{2}q$ and that of outgoing lepton $p + \frac{1}{2}q$ are on the mass shell so that p and q satisfy $p^2 = m^2 - \frac{1}{4}q^2$ and $p \cdot q = 0$. The magnetic moment amplitude from a vertex diagram can be extracted by using the projection operator $P_\nu(p,q)$.

4.2. Construction of the Feynman parametric integral

Usually, the QED amplitude of the perturbation theory is expressed as an integral of loop momenta flowing through the Feynman diagram. One of the ways to carry out the loop integral is to convert it into an integral of Feynman parameters z_i assigned to internal lines [70,86].

We consider a $2n$th-order lepton vertex diagram $\mathcal{G}$, which describes the scattering of an incoming lepton with momentum $p - q/2$ into an outgoing lepton with momentum $p + q/2$ by an external

magnetic field. $\mathcal{G}$ consists of $2n+1$ interaction vertices connected by $2n$ lepton propagators and n photon propagators, which are given in the form (in Feynman gauge):

$$i\frac{\not{p}_i + m_i}{p_i^2 - m_i^2}, \qquad \frac{-ig^{\mu\nu}}{p_i^2 - m_i^2}, \tag{4.5}$$

respectively. The momentum p_i may be decomposed as $p_i = k_i + q_i$, in which k_i is a linear combination of loop momenta, while q_i is a linear combination of external momenta. m_i is the mass associated with the line i, which are temporarily distinguished from each other. Of course, $m_i = 0$ for photons, but it is useful to give a small positive value in the intermediate steps to deal with the IR divergence, and take the limit $m_i = 0$ only at the end.

We introduce an operator D_i^μ by [88]

$$D_i^\mu \equiv \frac{1}{2}\int_{m_i^2}^{\infty} dm_i^2 \frac{\partial}{\partial q_{i\mu}} \tag{4.6}$$

and replace each numerator $\not{p}_i = \not{k}_i + \not{q}_i$ of lepton propagators (4.5) by $\not{D}_i$. Since D_i^μ does not depend on k_i explicitly, the numerators can be pulled out in front of the momentum integration as far as the integrand is adequately regularized.

The product of denominators is combined into one using the formula

$$\prod_{i=1}^{N}\frac{1}{\chi_i} = (N-1)!\left[\prod_{i=1}^{N}\int_0^1 dz_i\right]\delta\left(1-\sum_{i=1}^{N} z_i\right)\frac{1}{\left(\sum_{i=1}^{N} z_i\chi_i\right)^N}. \tag{4.7}$$

The sum $\sum_i z_i\chi_i$ is a quadratic form of loop momenta so that it can be diagonalized and integrated analytically with respect to the loop momenta. As a consequence, the amplitude is converted into an integral over Feynman parameters z_i, which is expressed in a concise form as

$$\Gamma_{\mathcal{G}}^{\nu} = \left(-\frac{1}{4}\right)^n (n-1)!\,\mathbb{F}^\nu \int (dz)_{\mathcal{G}}\,\frac{1}{U^2 V^n}, \tag{4.8}$$

where $N = 3n$ and

$$(dz)_{\mathcal{G}} = \prod_{i=1}^{N} dz_i\;\delta\left(1-\sum_{i=1}^{N} z_i\right), \tag{4.9}$$

$$V = \sum_{i=1}^{N} z_i(m_i^2 - q_i\cdot Q_i'), \tag{4.10}$$

$$Q_i'^{\,\mu} = -\frac{1}{U}\sum_{j=1}^{N} q_j^\mu z_j B_{ij}', \tag{4.11}$$

$$B_{ij}' = B_{ij} - \delta_{ij}\frac{U}{z_j}. \tag{4.12}$$

In Eq. (4.8) we have omitted the factor $(\alpha/\pi)^n$ for simplicity. U and B_{ij} are homogeneous polynomials of degree n and $n-1$ in Feynman parameters $\{z_i\}$, respectively, and are determined by the topology of a given diagram. Their precise definitions are given in Sect. 4.3. The operator $\mathbb{F}^\nu$ is of the form

$$\mathbb{F}^\nu = \gamma^{\alpha_1}(\not{D}_1 + m_1)\gamma^{\alpha_2}\ldots\gamma^\nu\ldots\gamma^{\alpha_{2n-1}}(\not{D}_{2n} + m_{2n})\gamma^{\alpha_{2n}}\prod_{k=1}^{n} g_{\alpha_{i_k}\alpha_{j_k}}, \tag{4.13}$$

where $\prod_k g_{\alpha_{i_k}\alpha_{j_k}}$ is a diagram-specific product. If $\mathcal{G}$ has closed lepton loops, $\mathbb{F}^\nu$ also contains appropriate trace operations.

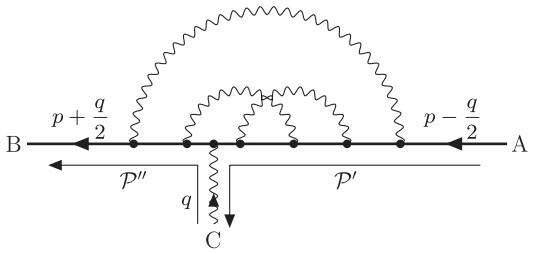

Fig. 6. A vertex diagram with given external momenta. A choice of paths $\mathcal{P}'$ and $\mathcal{P}''$ is shown.

Note that $\mathbb{F}^\nu$ can now be brought into the z-integral. The operator D_i^μ in $\mathbb{F}^\nu$ acts on $1/V^n$ as

$$D_i^\mu \frac{1}{V^n} = \frac{Q_i'^\mu}{V^n}, \tag{4.14}$$

$$D_i^\mu D_j^\nu \frac{1}{V^n} = \frac{Q_i'^\mu Q_j'^\nu}{V^n} - \frac{1}{2(n-1)} \frac{g^{\mu\nu} B'_{ij}}{U V^{n-1}}, \tag{4.15}$$

$$\begin{aligned} D_i^\mu D_j^\nu D_k^\rho \frac{1}{V^n} = {} & \frac{Q_i'^\mu Q_j'^\nu Q_k'^\rho}{V^n} \\ & - \frac{1}{2(n-1)} (g^{\mu\nu} B'_{ij} Q_k'^\rho + g^{\nu\rho} B'_{jk} Q_i'^\mu + g^{\rho\mu} B'_{ki} Q_j'^\nu) \frac{1}{U V^{n-1}}, \end{aligned} \tag{4.16}$$

$$\cdots .$$

The result of this operation may be summarized as a set of rules for a string of operators D_i^μ:

a) when $\not{D}_i$ and $\not{D}_j$ are "contracted", they are turned into a pair of γ^μ and γ_μ times a factor $(-\frac{1}{2} B'_{ij})$.
b) uncontracted D_i is replaced by Q'_i.

As a consequence the action of $\mathbb{F}^\nu$ produces a series of terms of the form

$$\mathbb{F}^\nu \frac{1}{U^2 V^n} = \frac{F_0^\nu}{U^2 V^n} + \frac{F_1^\nu}{U^3 V^{n-1}} + \cdots , \tag{4.17}$$

where F_k^ν are polynomials of B'_{ij} and Q'_i. The subscript k denotes the number of contractions. F_k^ν also includes an overall factor $\frac{1}{(n-1)(n-2)\cdots(n-k)}$.

All these procedures are summarized in our homemade integration table, which converts the momentum expression of the QED amplitude to the Feynman parameter expression.

It is convenient to replace vectors $Q_i'^\mu$ by scalar functions. Suppose the momentum $p^\mu - \frac{q^\mu}{2}$ enters the graph $\mathcal{G}$ at point A, follows the path $\mathcal{P}' = \mathcal{P}(AC)$, and leaves at C; and $p^\mu + \frac{q^\mu}{2}$ enters at C, follows the path $\mathcal{P}'' = \mathcal{P}(CB)$, and leaves at B (Fig. 6.) This can be expressed concisely by

$$q_j^\mu = \eta_{j\mathcal{P}'} \left(p^\mu - \frac{q^\mu}{2} \right) + \eta_{j\mathcal{P}''} \left(p^\mu + \frac{q^\mu}{2} \right), \tag{4.18}$$

where $\eta_{j\mathcal{P}'} = (1, -1, 0)$ according to whether the line j lies (along, against, outside of) the path $\mathcal{P}'$. It is similar for $\eta_{j\mathcal{P}''}$. Substituting Eq. (4.18) in Eq. (4.11) we obtain

$$Q_i'^\mu = A_i^{\mathcal{P}'} \left(p^\mu - \frac{q^\mu}{2} \right) + A_i^{\mathcal{P}''} \left(p^\mu + \frac{q^\mu}{2} \right), \tag{4.19}$$

where

$$A_i^{\mathcal{P}'} = -\frac{1}{U} \sum_{j=1}^{N} \eta_{j\mathcal{P}'} z_j B'_{ji}. \tag{4.20}$$

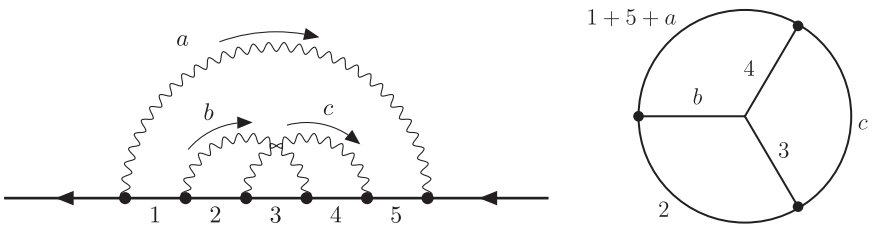

Fig. 7. A diagram (left) and the chain diagram derived from it (right).

It is similar for $A_i^{\mathcal{P}''}$. $A_i^{\mathcal{P}'}$ and $A_i^{\mathcal{P}''}$ will be called scalar currents associated with $p^\mu - \frac{q^\mu}{2}$ and $p^\mu + \frac{q^\mu}{2}$, respectively.

If we choose a path $\mathcal{P} = \mathcal{P}(AB)$ for p^μ, the corresponding scalar current becomes $A_i^{\mathcal{P}} = A_i^{\mathcal{P}'} + A_i^{\mathcal{P}''}$. Note that the choice of $\mathcal{P}(AB)$ is flexible as far as the end points A, B are fixed. Note also that $\mathcal{P}(AB)$ no longer depends on C.

4.3. Building blocks: B_{ij} and U

In our formalism, the parametric functions $B_{\alpha\beta}$ and U provide the basic building blocks, which are defined on the chain diagram corresponding to the diagram $\mathcal{G}$. Here α, β refer to the chains; a chain is a set of internal lines that carry the same loop momentum. The chain diagram is derived from $\mathcal{G}$ by amputating all the external lines and disregarding the distinction between the types of lines. Every chain is assumed to be properly directed. $B_{\alpha\beta}$ and U are homogeneous polynomials of degree $n-1$ and n, respectively, in $z_\alpha, \ldots$. They are the quantities that reflect the topological structure underlying the diagram $\mathcal{G}$.

$B_{\alpha\beta}$ and U can be obtained recursively by the following relations:

$$B_{\alpha\beta} = \sum_c \xi_{\alpha,c}\, \xi_{\beta,c}\, U_{\mathcal{G}/c}, \tag{4.21}$$

$$\xi_{\lambda,s} U = \sum_\alpha \xi_{\alpha,s} z_\alpha B_{\lambda\alpha}, \quad \text{for any } \lambda \in s, \tag{4.22}$$

starting from $U = z_\alpha$ for a single loop. Here the summation over c runs over all self-nonintersecting closed loops on $\mathcal{G}$. The loop matrix $\xi_{\alpha,c}$ is a projector of chain α to loop c, which takes the value $(1, -1, 0)$ according to whether α is (along, against, outside of) c. $U_{\mathcal{G}/c}$ is the U function for the reduced diagram $\mathcal{G}/c$ that is obtained from $\mathcal{G}$ by shrinking the loop c to a point. The loop s in Eq. (4.22) is an arbitrary closed loop.

Alternate and equivalent formulae for $B_{\alpha\beta}$ and U are obtained in the following manner. Suppose a set of independent self-nonintersecting loops (called a fundamental set of circuits) is given and define U_{st} by the summation over all chains by

$$U_{st} = \sum_\alpha z_\alpha\, \xi_{\alpha,s}\, \xi_{\alpha,t}, \tag{4.23}$$

where s, t are labels of circuits in the set. Then, U and $B_{\alpha\beta}$ are given by

$$U = \det_{st} U_{st}, \tag{4.24}$$

$$B_{\alpha\beta} = U \sum_{st} \xi_{\alpha,s}\, \xi_{\beta,t}\, (U^{-1})_{st}. \tag{4.25}$$

For a given diagram $\mathcal{G}$, first we have to identify the fundamental set of circuits, and construct the loop matrix $\xi_{\alpha,s}$. Then we can obtain U and $B_{\alpha\beta}$ according to the formulae above.

B_{ij} of the lines i, j is identical to $\eta_{i,\alpha}\eta_{j,\beta}B_{\alpha\beta}$, whose indices are such that $i \in \alpha$ and $j \in \beta$. The $\eta_{i,\alpha}$ takes the value 1 (-1) if the direction of the line i is parallel (anti-parallel) to the direction of the chain α. B_{ij} satisfies a so-called junction law on each vertex if the diagram $\mathcal{G}$ were regarded as an electric circuit in which the Feynman parameter z_i corresponds to the resistance of the line i:

$$\sum_i \epsilon_{vi} B_{ij} = 0 \tag{4.26}$$

for any vertex v and any internal line j, where ϵ_{vi} is called an incident matrix, defined by

$$\epsilon_{vi} = \begin{cases} 1 & \text{if the line } i \text{ enters the vertex } v, \\ -1 & \text{if the line } i \text{ leaves the vertex } v, \\ 0 & \text{otherwise.} \end{cases} \tag{4.27}$$

B_{ij} also satisfies a loop-law given by the following relation for arbitrary closed loop s and arbitrary line j:

$$\sum_i \xi_{i,s}\, z_i\, B'_{ji} = 0, \tag{4.28}$$

where $\xi_{i,s} = \eta_{i,\alpha}\xi_{\alpha,s}$ for $i \in \alpha$.

These relations reduce the number of independent elements among B_{ij}. They also provide consistency checks, which are useful in the actual calculations.

4.4. A set of vertex diagrams summed by the Ward–Takahashi identity

A set of vertex diagrams that are derived from a self-energy diagram by inserting an external vertex in every lepton propagator share many properties. Actually, we can go even further to relate those integrals to a single integral of the self-energy-like diagram through the Ward–Takahashi identity. This relation is useful when we consider higher-order calculations, because it substantially reduces the number of independent integrals.

It is well known that the proper vertex $\Gamma^\mu = \gamma^\mu + \Lambda^\mu$ and self-energy part Σ are related by the Ward–Takahashi identity

$$q_\mu \Lambda^\mu = -\Sigma\left(p + \frac{1}{2}q\right) + \Sigma\left(p - \frac{1}{2}q\right). \tag{4.29}$$

This relation also holds perturbatively for $\Sigma_\mathcal{G}$, representing the lepton self-energy diagram $\mathcal{G}$ and the sum of vertex diagrams $\Lambda_\mathcal{G}$ that are obtained by inserting an external vertex into $\mathcal{G}$ in every possible way. Differentiating both sides of Eq. (4.29) with respect to q^μ and taking the static limit $q \to 0$ of the external magnetic field, we have

$$\Lambda^\nu(p,q) \simeq -q^\mu \left[\frac{\partial \Lambda_\mu(p,q)}{\partial q_\nu}\right]_{q=0} - \frac{\partial \Sigma(p)}{\partial p_\nu}. \tag{4.30}$$

We may evaluate a_e starting from either side of this expression; a straightforward way is to calculate each vertex diagram individually and to gather them up according to the left-hand side, or else we can combine the set of vertices into one according to the right-hand side. For simple diagrams we evaluated the contribution to a_e by using both approaches. However, for complex diagrams with four or more photon corrections, we used the latter approach only.

In the Feynman parametric form, the $2n$th-order magnetic moment corresponding to the right-hand side of Eq. (4.30) can be written as [89]

$$M_{\mathcal{G}}^{(2n)} = \left(\frac{-1}{4}\right)^n (n-1)! \int (dz)_{\mathcal{G}} \left[\frac{\mathbb{E}+\mathbb{C}}{n-1}\frac{1}{U^2V^{n-1}} + (\mathbb{N}+\mathbb{Z})\frac{1}{U^2V^n}\right], \tag{4.31}$$

where $\mathbb{E}$, $\mathbb{C}$, $\mathbb{N}$, and $\mathbb{Z}$ are a set of operators defined as

$$\mathbb{N} = \frac{1}{4}\mathrm{Tr}[P_1^\nu p_\nu (2G\mathbb{F})], \tag{4.32}$$

$$\mathbb{E} = \frac{1}{4}\mathrm{Tr}[P_1^\nu \mathbb{E}_\nu], \tag{4.33}$$

$$\mathbb{C} = \frac{1}{4}\mathrm{Tr}[P_2^{\mu\nu} \mathbb{C}_{\mu\nu}], \tag{4.34}$$

$$\mathbb{Z} = \frac{1}{4}\mathrm{Tr}[P_2^{\mu\nu} \mathbb{Z}_{\mu\nu}]. \tag{4.35}$$

The magnetic projectors P_1^ν and $P_2^{\mu\nu}$ are derived from Eq. (4.4) by averaging over the direction of q_μ, and take the following forms:

$$P_1^\nu = \frac{1}{3}\gamma^\nu - \left(1 + \frac{4}{3}\frac{\not{p}}{m}\right)\frac{p^\nu}{m}, \tag{4.36}$$

$$P_2^{\mu\nu} = \frac{1}{3}\left(1+\frac{\not{p}}{m}\right)\left(g^{\mu\nu} - \gamma^\mu\gamma^\nu + \frac{p^\mu}{m}\gamma^\nu - \frac{p^\nu}{m}\gamma^\mu\right). \tag{4.37}$$

The operator $\mathbb{F}$ in (4.32) is the numerator part of the self-energy-like diagram $\mathcal{G}$ constructed with a similar form to Eq. (4.13):

$$\mathbb{F} = \gamma^{\alpha_1}(\not{D}_1 + m_1)\gamma^{\alpha_2}\ldots\gamma^{\alpha_{2n-1}}(\not{D}_{2n-1} + m_{2n-1})\gamma^{\alpha_{2n}} \prod_{k=1}^{n} g_{\alpha_{i_k}\alpha_{j_k}}, \tag{4.38}$$

which may contain appropriate trace operations if $\mathcal{G}$ has closed lepton loops. The operator $\mathbb{E}^\nu$ is defined by

$$\mathbb{E}^\nu = \frac{\partial\,\mathbb{F}}{\partial p_\nu} = \sum_{\text{all leptons}} A_i \mathbb{F}_i^\nu, \tag{4.39}$$

in which $\mathbb{F}_i^\nu$ is obtained from $\mathbb{F}$ by substituting in the ith line:

$$(\not{D}_i + m_i) \to \gamma^\nu. \tag{4.40}$$

The operator $\mathbb{Z}^{\mu\nu}$ is defined by

$$\mathbb{Z}^{\mu\nu} = \sum_j z_j \mathbb{Z}_j^{\mu\nu}. \tag{4.41}$$

The sum runs only over the lepton lines into which the external photon line is inserted. $\mathbb{Z}_j^{\mu\nu}$ is obtained from $\mathbb{F}$ by substituting in the jth line:

$$(\not{D}_j + m_j) \to \frac{1}{2}[\gamma^\mu\gamma^\nu(\not{D}_j + m_j) - (\not{D}_j + m_j)\gamma^\nu\gamma^\mu]. \tag{4.42}$$

The operator $\mathbb{C}^{\mu\nu}$ is defined by

$$\mathbb{C}^{\mu\nu} = \sum_{i<j} C_{ij}\mathbb{F}_{ij}^{\mu\nu}, \tag{4.43}$$

where i and j refer to *all* lepton lines. C_{ij} is defined by

$$C_{ij} = \frac{1}{U^2} \sum_{k<l} z_k z_l (B'_{ik} B'_{jl} - B'_{il} B'_{jk}), \tag{4.44}$$

where the sums over k, l are taken for the lepton lines that belong to the path on which the momentum q^ν of the external magnetic field flows. $\mathbb{F}_{ij}^{\mu\nu}$ is obtained from $\mathbb{F}$ by substituting in the ith and jth lepton lines:

$$(\not{D}_i + m_i), (\not{D}_j + m_j) \to \gamma^\mu, \gamma^\nu. \tag{4.45}$$

G is given by

$$G = \sum_i z_i A_i, \tag{4.46}$$

where the summation runs over the lepton lines on which the external momentum p^μ flows (depending on the choice of path $\mathcal{P}(AB)$ for the scalar currents).

5. Subtractive UV renormalization procedure

The treatment of UV and IR divergences in the Feynman parametric formalism was originally described in Ref. [90]. It turns out that the UV treatment in Ref. [90] can be easily translated to the automation algorithm of Ref. [35] and implemented in gencode*N*.

5.1. General remarks on UV divergence

The amplitude constructed in the previous section is divergent in general. The divergences must be eliminated before carrying out numerical integration. The UV divergence arises when one or more loop momenta go to infinity. This is seen in Feynman parameter space as all parameters z_i that belong to loops of a subdiagram go to zero simultaneously. This allows power-counting rules for identifying the emergence of divergences in a manner similar to ordinary momentum integration.

We adopt here the subtractive on-shell renormalization. The renormalization constants that appear in QED are the mass renormalization constant δm, the wavefunction renormalization constant B, and the vertex renormalization constant L. They are determined on the mass shell, and thus the coupling constant e and the mass of the lepton m are guaranteed to be the physical ones.

To perform renormalization numerically one must prepare the subtraction term as an integral over the same domain of integration as the original unrenormalized amplitude, and to perform point-wise subtraction in which singularities of the original integrand are canceled point-by-point on the parameter space before the integration is carried out. To achieve this, the renormalization constant L_m and the lower-order $g-2$ term M_{n-m} must both be expressed in the parametric integral and combined by the Feynman integral formula. It is found, however, that the integral is not easily manageable if L_m is treated as a whole. Instead, we adopt the following intermediate renormalization scheme, in which L_m is split as

$$L_m = L_m^{\mathrm{UV}} + \widetilde{L_m}, \tag{5.1}$$

and only the UV-divergent part L_m^{UV} is subtracted.

The subtraction term $L_m^{\mathrm{UV}} M_{n-m}$ is found to have a term-by-term correspondence with the UV-divergent term of the original integral M_n, and thus cancels the UV singularities. It is identified from the original integrand by simple power-counting rules. This procedure is formulated as K-operation. The treatment of the UV divergence of the self-energy subdiagram is slightly more complicated; see Refs. [89] and [87] and Eq. (5.37) for details.

The UV-finite part of the renormalization constant is treated separately together with similar terms from other diagrams. This step is called the residual renormalization, examples of which are discussed in Sect. 7.

In this section we shall describe how to construct the intermediate renormalization term via K-operation. It is shown that the subtraction term factorizes exactly into the UV-divergent part of the mth-order renormalization constant and M_{n-m} by construction. This feature is crucial for the subsequent operation when the UV divergence arises from more than one divergent subdiagram. The factorization property is also significant for the residual renormalization step in the sense that the highest order of the residual part decreases by two, e.g., for the 10th-order diagrams it is sufficient to consider at most eighth-order terms. Therefore the evaluation of the residual part reduces to lower-order integrals.

5.2. *UV-divergent subdiagram*

The UV divergence associated with the subdiagram $\mathcal{S}$ is caused by the simultaneous limits $k_i \to \infty$ of all loop momenta k_i, $i \in \mathcal{S}$. In the parametric representation (4.31) this is translated into the vanishing of the denominator U at a boundary of Feynman parameter space where[1]

$$z_i = \begin{cases} \mathcal{O}(\epsilon) & i \in \mathcal{S}, \\ \mathcal{O}(1) & \text{otherwise}, \end{cases} \tag{5.2}$$

with $\epsilon \to 0$.

To find how UV divergence arises from a subdiagram $\mathcal{S}$ consisting of $N_\mathcal{S}$ internal lines and $n_\mathcal{S}$ loops, consider the integration domain (5.2). In the limit $\epsilon \to 0$, the homogeneous polynomials in the integrand behave as follows (see Sect. 5.4 for proofs):

$$U = \mathcal{O}(\epsilon^{n_\mathcal{S}}), \quad V = \mathcal{O}(1), \tag{5.3}$$

and

$$B_{ij} = \begin{cases} \mathcal{O}(\epsilon^{n_\mathcal{S}-1}) & \text{if } i, j \in \mathcal{S}, \\ \mathcal{O}(\epsilon^{n_\mathcal{S}}) & \text{otherwise}. \end{cases} \tag{5.4}$$

Let $m_\mathcal{S}$ be the maximum number of contractions of operator D_i within $\mathcal{S}$. Simple power-counting shows that the m-contracted term of $M^{(2n)}$ in Eq. (4.31) is divergent if and only if

$$N_\mathcal{S} - 2n_\mathcal{S} \le \min(m, m_\mathcal{S}), \tag{5.5}$$

where $\min(m, m_\mathcal{S})$ means the lesser of m and $m_\mathcal{S}$. If $\mathcal{S}$ is a vertex part, we have $N_\mathcal{S} = 3n_\mathcal{S}$ and $m_\mathcal{S} = n_\mathcal{S}$. If $\mathcal{S}$ is a self-energy part, we have $N_\mathcal{S} = 3n_\mathcal{S} - 1$ and $m_\mathcal{S} = n_\mathcal{S} - 1$. In both cases Eq. (5.5) is satisfied only for $m \ge m_\mathcal{S}$. Let us denote the UV limit (5.2) of U and B_{ij} as $[U]^\mathcal{S}_{\mathrm{UV}}$ and $[B_{ij}]^\mathcal{S}_{\mathrm{UV}}$.

5.3. *K-operation*

We are now ready to set up the rules of K-operation for constructing the intermediate renormalization term. Let $\mathcal{G}/\mathcal{S}$ denote a residual diagram that is obtained from $\mathcal{G}$ by shrinking a subdiagram $\mathcal{S}$ to a point.

[1] The overall divergence of a self-energy-like diagram drops automatically after projecting out the magnetic moment contribution.

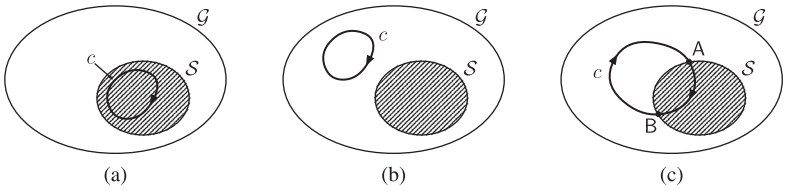

Fig. 8. A closed loop c running in $\mathcal{G}$. Reproduced with permission from [35].

The K-operation K_S is defined as follows.

1. In Eq. (4.31), collect all terms that are maximally contracted within the subdiagram S.
2. Replace U, B_{ij}, C_{ij}, and A_i appearing in the integrand with their UV limits, $[U]^{\mathcal{S}}_{\mathrm{UV}}$, $[B_{ij}]^{\mathcal{S}}_{\mathrm{UV}}$, $[C_{ij}]^{\mathcal{S}}_{\mathrm{UV}}$, and $[A_i]^{\mathcal{S}}_{\mathrm{UV}}$, respectively.
3. Replace V with $V_{\mathcal{S}} + V_{\mathcal{G}/\mathcal{S}}$, where $V_{\mathcal{S}}$ and $V_{\mathcal{G}/\mathcal{S}}$ are V functions of $\mathcal{S}$ and $\mathcal{G}/\mathcal{S}$, respectively.
4. Attach an overall minus sign.

A naive UV limit gives $V \to V_{\mathcal{G}/\mathcal{S}}$ instead of step (3). Since $V_{\mathcal{S}}$ is a higher-order term in ϵ, its addition in step (3) does not affect the UV limit. But it is crucial because it enables us to satisfy the exact factorization of the renormalization constant and the rest of the amplitude required by the standard renormalization [90]. Furthermore, it enables us to avoid the spurious IR divergence that $V_{\mathcal{G}/\mathcal{S}}$ alone might develop in other parts of the integration domain.

5.4. UV limit of building blocks U, B_{ij}, and C_{ij}

Let us now describe step by step how the building blocks of the integrand behave in the UV limit (5.2). It is found that each of them factorizes into two parts, one of which depends solely on the subdiagram $\mathcal{S}$, and the other on the residual diagram $\mathcal{G}/\mathcal{S}$ alone.

The U function is a homogeneous polynomial of Feynman parameters of degree n defined by Eq. (4.24), which has a simple behavior in the limit (5.2) [91]

$$[U]^{\mathcal{S}}_{\mathrm{UV}} = U_{\mathcal{S}}\, U_{\mathcal{G}/\mathcal{S}} \quad (= \mathcal{O}(\epsilon^{n_{\mathcal{S}}})). \tag{5.6}$$

In order to obtain the UV limit of B_{ij}, let us note that for $i \in \alpha$, $j \in \beta$, $B_{\alpha\beta}$ of Eq. (4.21) can be written as

$$B_{ij} = \sum_c \xi_{i,c}\, \xi_{j,c}\, U_{\mathcal{G}/c}. \tag{5.7}$$

Since $(\mathcal{G}/c) \cap \mathcal{S} = \mathcal{S}/(c \cap \mathcal{S})$ and $(\mathcal{G}/c)/\mathcal{S} = \mathcal{G}/(c \cup \mathcal{S})$, the UV limit of $U_{\mathcal{G}/c}$ becomes

$$[U_{\mathcal{G}/c}]^{\mathcal{S}}_{\mathrm{UV}} = U_{\mathcal{S}/(c\cap\mathcal{S})}\, U_{\mathcal{G}/(c\cup\mathcal{S})}. \tag{5.8}$$

The explicit form depends on how loop c runs in $\mathcal{G}$:

Case (a) c is contained in $\mathcal{S}$ (i.e. $c \subseteq \mathcal{S}$); see Fig. 8 (a).
In this case $\mathcal{S}/(c \cap \mathcal{S}) = \mathcal{S}/c$ and $\mathcal{G}/(c \cup \mathcal{S}) = \mathcal{G}/\mathcal{S}$. Therefore

$$[U_{\mathcal{G}/c}]^{\mathcal{S}}_{\mathrm{UV}} = U_{\mathcal{S}/c}\, U_{\mathcal{G}/\mathcal{S}} \quad (= \mathcal{O}(\epsilon^{n_{\mathcal{S}}-1})). \tag{5.9}$$

The power of ϵ decreases by 1 since $\mathcal{S}/c$ has one less loop than $\mathcal{S}$.

Case (b) c runs outside of $\mathcal{S}$ (i.e. $c \subseteq (\mathcal{G} - \mathcal{S})$). Here, $\mathcal{G} - \mathcal{S}$ denotes a diagram obtained from $\mathcal{G}$ by eliminating all lines that belong to $\mathcal{S}$; see Fig. 8 (b).
In this case $\mathcal{S}/(c \cap \mathcal{S}) = \mathcal{S}$ and $\mathcal{G}/(c \cup \mathcal{S}) = (\mathcal{G}/\mathcal{S})/c$. Therefore

$$[U_{\mathcal{G}/c}]^{\mathcal{S}}_{\mathrm{UV}} = U_{\mathcal{S}}\, U_{(\mathcal{G}/\mathcal{S})/c} \quad (= \mathcal{O}(\epsilon^{n_{\mathcal{S}}})). \tag{5.10}$$

Case (c) c is contained in both $\mathcal{S}$ and $\mathcal{G}-\mathcal{S}$ (i.e. $c\cap\mathcal{S}\neq\emptyset$ and $c\cap(\mathcal{G}-\mathcal{S})\neq\emptyset$); see Fig. 8 (c). In this case $c\cap\mathcal{S}$ is an open self-nonintersecting path within $\mathcal{S}$. It does not change the number of loops in $\mathcal{S}$ when the path is shrunken to a point. Therefore the scaling behavior is

$$[U_{\mathcal{G}/c}]^{\mathcal{S}}_{\mathrm{UV}}=\mathcal{O}(\epsilon^{n_{\mathcal{S}}}), \tag{5.11}$$

though exact factorization does not occur.

From these observations and Eq. (5.7), we find the following behavior of B_{ij} in the UV limit.

I) B_{ij} for $i,j\in\mathcal{S}$.
The closed loops appearing in the sum in Eq. (5.7) fall into either of the cases (a) or (c); the former gives the leading contribution whereas the latter does not in the limit (5.2). Thus we have

$$\begin{aligned}[B_{ij}]^{\mathcal{S}}_{\mathrm{UV}}&=\sum_{c'\subseteq\mathcal{S}}\xi_{i,c'}\,\xi_{j,c'}\,U_{\mathcal{S}/c'}\,U_{\mathcal{G}/\mathcal{S}}\\&=B^{\mathcal{S}}_{ij}\,U_{\mathcal{G}/\mathcal{S}},\end{aligned} \tag{5.12}$$

where the superscript $\mathcal{S}$ denotes that $B^{\mathcal{S}}_{ij}$ is defined for the subdiagram $\mathcal{S}$.

II) B_{ij} for $i,j\in\mathcal{G}/\mathcal{S}$.
The closed loops appearing in the sum in (5.7) fall into either of the cases (b) or (c), both of which give the same order of contributions:

$$[B_{ij}]^{\mathcal{S}}_{\mathrm{UV}}=\sum_{c'\text{ in case (b)}}\xi_{i,c'}\,\xi_{j,c'}\,U_{\mathcal{G}/c'}+\sum_{c''\text{ in case (c)}}\xi_{i,c''}\,\xi_{j,c''}\,U_{\mathcal{G}/c''}. \tag{5.13}$$

In the first term on the right-hand side, the sum over the closed loops $c'\subseteq(\mathcal{G}-\mathcal{S})$ is equivalent to the sum over loops in $\mathcal{G}/\mathcal{S}-\{s\}$, namely the loops in the residual diagram $\mathcal{G}/\mathcal{S}$ that does not pass through point s, where s denotes a point into which the subdiagram $\mathcal{S}$ has shrunk. Therefore, the first term becomes

$$U_{\mathcal{S}}=\sum_{c'\subseteq(\mathcal{G}/\mathcal{S}-\{s\})}\xi_{i,c'}\,\xi_{j,c'}\,U_{(\mathcal{G}/\mathcal{S})/c'}. \tag{5.14}$$

In the second term, the closed loop c'' passing through points $A,B\in\mathcal{S}\cap(\mathcal{G}-\mathcal{S})$ is decomposed into two open paths $\mathcal{P}(AB)=c''\cap\mathcal{S}$ and $\mathcal{P}'(AB)=c''\cap(\mathcal{G}-\mathcal{S})$. The sum over c'' becomes the sum over a choice of points A, B and open paths $\mathcal{P}(AB)$, $\mathcal{P}'(AB)$. It is shown [91] that $U_{\mathcal{S}/\mathcal{P}}$ satisfies

$$U_{\mathcal{S}}=\sum_{\mathcal{P}(AB)}U_{\mathcal{S}/\mathcal{P}}. \tag{5.15}$$

On the other hand, the path $\mathcal{P}'(AB)$ becomes a closed loop in $\mathcal{G}/\mathcal{S}$ that passes through the point s to which S has shrunk. Thus the second term becomes

$$U_{\mathcal{S}}=\sum_{c''\subseteq\mathcal{G}/\mathcal{S},\ c''\ni s}\xi_{i,c''}\,\xi_{j,c''}\,U_{(\mathcal{G}/\mathcal{S})/c''}. \tag{5.16}$$

From Eqs. (5.14) and (5.16) the UV limit of B_{ij} is

$$[B_{ij}]^{\mathcal{S}}_{\mathrm{UV}}=B^{\mathcal{G}/\mathcal{S}}_{ij}\,U_{\mathcal{S}}\quad i,j\in(\mathcal{G}/\mathcal{S}). \tag{5.17}$$

III) B_{mj} for $m\in\mathcal{S}$ and $j\in\mathcal{G}/\mathcal{S}$.

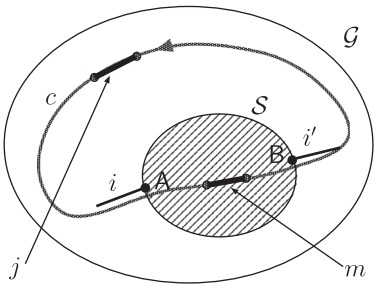

Fig. 9. A self-energy subdiagram $\mathcal{S}$ and a closed loop c that passes through $m \in \mathcal{S}$ and $j \in \mathcal{G}/\mathcal{S}$. Reproduced with permission from [35].

This case is relevant only when $\mathcal{S}$ is a self-energy subdiagram, since for the vertex subdiagram case the leading contribution comes from the terms in which all lepton lines in $\mathcal{S}$ are contracted with each other.

We denote the lines that are attached to the subdiagram $\mathcal{S}$ by i and i'. (See Fig. 9.) The closed loop c that contains the lines $m \in \mathcal{S}$ and $j \in \mathcal{G}/\mathcal{S}$ passes through i and i'. The sum over loops c is decomposed into the sum over $\mathcal{P} = c \cap \mathcal{G}$ and $\mathcal{P}' = c \cap (\mathcal{G} - \mathcal{S})$. It is shown [91] that

$$\sum_{\mathcal{P}} \xi_{m,\mathcal{P}}\, U_{\mathcal{S}/\mathcal{P}} = U_{\mathcal{S}}\, A^{\mathcal{S}}_{m}, \tag{5.18}$$

where $A^{\mathcal{S}}_{m}$ is a scalar current on the line m of the diagram $\mathcal{S}$. The path $\mathcal{P}'$ turns into a closed path c' after shrinking $\mathcal{S}$ to a point that passes through the line $i \in \mathcal{G}/\mathcal{S}$. Therefore B_{mj} becomes

$$\begin{aligned}[B_{mj}]^{\mathcal{S}}_{\mathrm{UV}} &= \left(\sum_{c'} \xi_{j,c'}, \xi_{i,c'}\, U_{(\mathcal{G}/\mathcal{S})/c'} \right) U_{\mathcal{S}}\, A^{\mathcal{S}}_{m} \\ &= B^{\mathcal{G}/\mathcal{S}}_{ij}\, A^{\mathcal{S}}_{m}\, U_{\mathcal{S}}. \end{aligned} \tag{5.19}$$

The UV limit of the scalar current A_j follows from Eq. (4.20), where the path $\mathcal{P}$ (that replaces P') is taken arbitrarily between two points attached to external lines. We can always choose the path to avoid the line j so that B'_{ij} in Eq. (4.20) becomes B_{ij}.

When $\mathcal{S}$ is a vertex subdiagram, it is sufficient to consider only A_j with $j \in \mathcal{G}/\mathcal{S}$, since in the leading contributions of the integrand all the lepton lines in $\mathcal{S}$ are contracted and there is no operator D_i left to be turned into scalar current. The sum in Eq. (4.20) consists of two parts, one from $\mathcal{P}' = \mathcal{P} \cap \mathcal{S}$ and the other from $\mathcal{P}'' = \mathcal{P} \cap (\mathcal{G} - \mathcal{S})$. In the limit (5.2) the scaling behavior (5.4) shows that the former part gives a sub-leading contribution. Therefore, using Eq. (5.17), we obtain

$$\begin{aligned}[A_j]^{\mathcal{S}}_{\mathrm{UV}} &= -\frac{1}{U_{\mathcal{G}/\mathcal{S}}} \sum_{i \in \mathcal{G}/\mathcal{S}} \eta_{i\mathcal{P}''}\, z_i\, B^{\mathcal{G}/\mathcal{S}}_{ij} \\ &= A^{\mathcal{G}/\mathcal{S}}_{j}. \end{aligned} \tag{5.20}$$

When $\mathcal{S}$ is a self-energy subdiagram, the scalar currents of both $j \in \mathcal{G}/\mathcal{S}$ and $j \in \mathcal{S}$ are relevant.

Case (a) A_j for $j \in \mathcal{G}/\mathcal{S}$.

The same argument for the UV limit as in the vertex subdiagram applies to this case, which leads to

$$[A_j]^{\mathcal{S}}_{\mathrm{UV}} = A^{\mathcal{G}/\mathcal{S}}_{j}. \tag{5.21}$$

Case (b) A_m for $m \in \mathcal{S}$.

We choose the path $\mathcal{P}$ so that it avoids $\mathcal{S}$. Then all B_{im} in (4.20) fall into type III, whose UV limits are given by Eq. (5.19). Therefore,

$$[A_m]^{\mathcal{S}}_{\rm UV} = -\frac{1}{U_{\mathcal{G}/\mathcal{S}}} \sum_{k\in\mathcal{P}} z_k \, B^{\mathcal{G}/\mathcal{S}}_{ik} A^{\mathcal{S}}_m$$
$$= A^{\mathcal{G}/\mathcal{S}}_i \, A^{\mathcal{S}}_m, \tag{5.22}$$

where i is the line adjacent to $\mathcal{S}$.

We recall that C_{ij} is derived from the part

$$-q^\mu \left[\frac{\partial \Lambda_\mu}{\partial q_\nu}\right]_{q=0} \tag{5.23}$$

of Eq. (4.30) with the external vertex inserted into the line j and differentiated with respect to the external momentum q_ν flowing through the line i. When $\mathcal{S}$ is a vertex subdiagram, C_{ij} for i or j in $\mathcal{S}$ has no overall UV divergence, since $\mathcal{S}$ has, effectively speaking, four legs: one photon line attached to the external vertex, the other internal photon line that is connected to $\mathcal{G}/\mathcal{S}$, and two internal lepton lines. So it is sufficient to consider the cases $i, j \in \mathcal{G}/\mathcal{S}$, in which the UV limit of C_{ij} becomes

$$[C_{ij}]^{\mathcal{S}}_{\rm UV} = \frac{1}{U_{\mathcal{G}/\mathcal{S}}} C^{\mathcal{G}/\mathcal{S}}_{ij}. \tag{5.24}$$

When $\mathcal{S}$ is a self-energy subdiagram, the definition (4.44) of C_{ij} and the UV limits of B_{ij} lead to the following forms:

$$[C_{jk}]^{\mathcal{S}}_{\rm UV} = \frac{1}{U_{\mathcal{G}/\mathcal{S}}} C^{\mathcal{G}/\mathcal{S}}_{jk} \quad j,k \in \mathcal{G}/\mathcal{S}, \tag{5.25}$$

$$[C_{fg}]^{\mathcal{S}}_{\rm UV} = \frac{1}{U_{\mathcal{S}}} C^{\mathcal{S}}_{fg} + \frac{1}{U_{\mathcal{S}}} \left(A^{\mathcal{S}}_g \sum_{h\in\mathcal{S}} z_h B'^{\mathcal{S}}_{fh} - A^{\mathcal{S}}_f \sum_{h\in\mathcal{S}} z_h B'^{\mathcal{S}}_{gh} \right)$$
$$\times \frac{1}{U_{\mathcal{G}/\mathcal{S}}} \sum_{j\in\mathcal{G}/\mathcal{S}} z_j B'^{\mathcal{G}/\mathcal{S}}_{ij}, \quad f,g \in \mathcal{S}, \tag{5.26}$$

$$[C_{fj}]^{\mathcal{S}}_{\rm UV} = \frac{1}{U_{\mathcal{G}/\mathcal{S}}} A^{\mathcal{S}}_f \, C^{\mathcal{G}/\mathcal{S}}_{ij} + \frac{1}{U_{\mathcal{S}}} \sum_{g\in\mathcal{S}} z_g B'^{\mathcal{S}}_{fg} \frac{1}{U_{\mathcal{G}/\mathcal{S}}} \sum_{k\in\mathcal{G}/\mathcal{S}} z_k B'^{\mathcal{G}/\mathcal{S}}_{jk} \quad f \in \mathcal{S}, \, j \in \mathcal{G}/\mathcal{S}, \tag{5.27}$$

where i is the line adjacent to $\mathcal{S}$.

5.5. *Factorization property of the UV subtraction term*

Now we proceed to examine the UV subtraction term along the steps of K-operation to see that it factorizes into two parts. For simplicity we consider a vertex part $\Gamma^\nu_{\mathcal{G}}$ defined in Eqs. (4.8) and (4.17), though the arguments apply to the general cases.

Suppose the UV-divergent subdiagram $\mathcal{S}$ is a vertex subdiagram. In step (1) of K-operation we pick up the terms that are maximally contracted within $\mathcal{S}$. Such a term among the terms with k contractions, $\frac{F_k}{U^{2+k}V^{n-k}}$, has the form:

$$\frac{1}{U^2 V^{n-k}} \underbrace{\left\{ \left(\frac{B_{ij}}{U}\right) \cdots \right\}}_{i,j\in\mathcal{S}} \underbrace{\left\{ \left(\frac{B_{i'j'}}{U}\right) \cdots A_{l'} \cdots \right\}}_{i',j',l'\in\mathcal{G}/\mathcal{S}}. \tag{5.28}$$

The first factor in the braces is a product of the B_{ij} with $i, j \in \mathcal{S}$, while the second factor is a product that consists of $(k - n_{\mathcal{S}})$ $B_{i'j'}$ and several scalar currents whose indices i', j' are in $\mathcal{G}/\mathcal{S}$.

In step (2) we consider the UV limit (5.2). This is achieved by replacing the building blocks U, B_{ij}, and A_j by their UV limits, $[U]^{\mathcal{S}}_{\rm UV}$, $[B_{ij}]^{\mathcal{S}}_{\rm UV}$, and $[A_j]^{\mathcal{S}}_{\rm UV}$, respectively. Then Eq. (5.28) turns into

$$\underbrace{\frac{1}{U_{\mathcal{S}}^2}\left\{\left(\frac{B^{\mathcal{S}}_{ij}}{U_{\mathcal{S}}}\right)\cdots\right\}}_{\equiv g[\mathcal{S}]}\underbrace{\frac{1}{U_{\mathcal{G}/\mathcal{S}}^2}\left\{\left(\frac{B^{\mathcal{G}/\mathcal{S}}_{i'j'}}{U_{\mathcal{G}/\mathcal{S}}}\right)\cdots A^{\mathcal{G}/\mathcal{S}}_{l'}\cdots\right\}}_{\equiv g[\mathcal{G}/\mathcal{S}]}\frac{1}{V_{\mathcal{G}/\mathcal{S}}^{n-k}}. \tag{5.29}$$

The first part depends only on z_i with $i \in \mathcal{S}$, which we denote by $g[\mathcal{S}]$. The second part depends only on z_i with $i \in \mathcal{G}/\mathcal{S}$. It is denoted similarly by $g[\mathcal{G}/\mathcal{S}]$. In the naive UV limit, V leads to $V_{\mathcal{G}/\mathcal{S}}$.

In step (3) $V_{\mathcal{G}/\mathcal{S}}$ is replaced by $V_{\mathcal{S}} + V_{\mathcal{G}/\mathcal{S}}$. The integral now becomes

$$\int (dz)_{\mathcal{G}}\, g[\mathcal{S}]\, g[\mathcal{G}/\mathcal{S}]\frac{1}{(V_{\mathcal{S}} + V_{\mathcal{G}/\mathcal{S}})^{n-k}}. \tag{5.30}$$

We shall see that it factorizes into $\mathcal{S}$ and $\mathcal{G}/\mathcal{S}$ parts. Firstly, the identity

$$1 = \int_0^1 \frac{ds}{s}\,\delta\left(1 - \frac{z_{\mathcal{S}}}{s}\right)\int_0^1 \frac{dt}{t}\,\delta\left(1 - \frac{z_{\mathcal{G}/\mathcal{S}}}{t}\right) \tag{5.31}$$

is inserted into the integral, where $z_{\mathcal{S}}$ and $z_{\mathcal{G}/\mathcal{S}}$ are defined by $z_{\mathcal{S}} = \sum_{i\in\mathcal{S}} z_i$ and $z_{\mathcal{G}/\mathcal{S}} = \sum_{i\in\mathcal{G}/\mathcal{S}} z_i$, respectively. Secondly, we rescale the Feynman parameters as follows:

$$\begin{aligned} z_i &\to s z_i \quad i \in \mathcal{S} \\ z_i &\to t z_i \quad i \in \mathcal{G}/\mathcal{S}. \end{aligned} \tag{5.32}$$

Since the V-functions are homogeneous polynomials of degree 1, they scale in such a manner as $V_{\mathcal{S}} \to s\, V_{\mathcal{S}}$ and $V_{\mathcal{G}/\mathcal{S}} \to t\, V_{\mathcal{G}/\mathcal{S}}$. Other parts of the integrand and the integration measure also scale accordingly.

Then, using the Feynman integral formula

$$\Gamma(k+l)\int_0^1 ds\, dt\, \delta(1-s-t)\frac{s^{k-1}t^{l-1}}{(sA+tB)^{k+l}} = \frac{\Gamma(k)}{A^k}\,\frac{\Gamma(l)}{B^l}, \tag{5.33}$$

the integral is shown to be factorized into two parts:

$$\begin{aligned} &\int dz_{\mathcal{S}}\,\delta(1-z_{\mathcal{S}})\, g[\mathcal{S}]\int dz_{\mathcal{G}/\mathcal{S}}\,\delta(1-z_{\mathcal{G}/\mathcal{S}})\, g[\mathcal{G}/\mathcal{S}]\int ds\, dt\,\delta(1-s-t)\,\frac{s^{\alpha-1}t^{\beta-1}}{(s\,V_{\mathcal{S}} + t\,V_{\mathcal{G}/\mathcal{S}})^{\alpha+\beta}} \\ &\quad = \int (dz)_{\mathcal{S}}\,\frac{g[\mathcal{S}]}{V_{\mathcal{S}}^{\alpha}} \times \int (dz)_{\mathcal{G}/\mathcal{S}}\,\frac{g[\mathcal{G}/\mathcal{S}]}{V_{\mathcal{G}/\mathcal{S}}^{\beta}}, \end{aligned} \tag{5.34}$$

where α and β are constants determined by the rescaling (5.32).

Based on these observations the whole integral of the vertex part $\Gamma^{\nu}_{\mathcal{G}}$ is shown to be factorized in the UV limit as

$$\mathsf{K}_{\mathcal{S}}\Gamma^{\nu}_{\mathcal{G}} = L^{\rm UV}_{\mathcal{S}}\Gamma^{\nu}_{\mathcal{G}/\mathcal{S}}, \tag{5.35}$$

where $L^{\rm UV}_{\mathcal{S}}$ is the UV-divergent part of the vertex renormalization constant $L_{\mathcal{S}}$ and $\Gamma^{\nu}_{\mathcal{G}/\mathcal{S}}$ is the vertex part of the residual diagram $\mathcal{G}/\mathcal{S}$.

When $\mathcal{S}$ is a self-energy subdiagram, the factorization is not apparent because not all $\not{D}_m$ with $m \in \mathcal{S}$ are contracted. From Eqs. (5.19) and (5.22) we can symbolically write the uncontracted $\not{D}_m$ as

$$[\not{D}_m]^{\mathcal{S}}_{\rm UV} = A^{\mathcal{S}}_m \not{D}^{\mathcal{G}/\mathcal{S}}_{i''}, \tag{5.36}$$

where i'' is a fictitious line related to i and i'. After a little algebra, one finds [87,89]

$$\mathsf{K}_{\mathcal{S}}\Gamma^{\nu}_{\mathcal{G}} = \delta m^{\rm UV}_{\mathcal{S}}\Gamma^{\nu}_{\mathcal{G}/\mathcal{S}(i^*)} + B^{\rm UV}_{\mathcal{S}}\Gamma^{\nu}_{\mathcal{G}/[\mathcal{S},i']}, \tag{5.37}$$

where $\delta m^{\rm UV}_{\mathcal{S}}$ is the UV-divergent part of the mass renormalization constant $\delta m_{\mathcal{S}}$ and $B^{\rm UV}_{\mathcal{S}}$ is that of the wavefunction renormalization constant $B_{\mathcal{S}}$. $\mathcal{G}/\mathcal{S}(i^*)$ denotes the diagram obtained by shrinking $\mathcal{S}$ to a point, where i^* indicates a two-point vertex between lines i and i'. $\mathcal{G}/[\mathcal{S}, i']$ denotes the diagram derived from $\mathcal{G}$ by shrinking $\mathcal{S}$ to a point and eliminating the line i'. It can be reduced to the form $\Gamma^{\nu}_{\mathcal{G}/\mathcal{S}}$ after integration by parts with respect to z_i.

Nested UV singularities are handled by following Zimmermann's forest formula [92]. The UV divergence of the diagram is identified by a structure called a forest, which is a set of non-overlapping UV-divergent subdiagrams[2]. This can be easily translated to successive applications of $\mathsf{K}_{\mathcal{S}_i}$-operations. Then, we can obtain the UV-divergence-free magnetic moment amplitude

$$M^{\rm R}_{\mathcal{G}} = \sum_f (-\mathsf{K}_{\mathcal{S}_i}) \times (-\mathsf{K}_{\mathcal{S}_j}) \times \cdots M_{\mathcal{G}}, \tag{5.38}$$

where $\mathcal{S}_i$ is one of the subdiagrams belonging to the forest f and the sum is taken over all forests f constructed for the diagram $\mathcal{G}$.

6. Treatment of IR divergences

The UV separation method in Ref. [90] is easily implemented in the automation code gencode*N*. However, the IR treatment is not so simple. In Ref. [90], both UV and IR terms are derived by using power-counting rules. The UV divergence occurs as the leading term of the power-counting. The separation of IR divergences in Ref. [90] is, however, based on power-counting through elaborate examination of the individual integrands, and thus it makes automated treatment difficult. Therefore, we invented another approach based on the graphical observation. Here, we describe our new IR treatment , which was reported in Ref. [36].

6.1. General remarks on IR divergence

The magnetic form factor is free from UV and IR divergences once it is fully renormalized. However, individual diagrams suffer from IR divergences that cancel out only after all diagrams are combined.

The root cause of IR divergence is the vanishing of the denominator of the photon propagator $1/k^2$ in the limit $k \to 0$. This is, however, not the sufficient condition since it gives a finite result on integration over the 4-dimensional momentum k. In order that it becomes divergent, it must be enhanced by vanishing of the denominators of at least two lepton propagators due to some kinematical constraints. Typically, this happens when the momentum of each of these lepton propagators is constrained by sharing a three-point vertex with the soft photon and an external on-shell lepton line. When the external momentum p is constrained by the on-shell condition $p^2 = m^2$, the lepton

[2] "Non-overlapping" means that a pair of subdiagrams is disjoint, or one of the pair is included in the other.

propagator in question behaves as

$$\frac{1}{(p+k)^2-m^2}=\frac{1}{2p\cdot k+k^2}\sim\frac{1}{2p\cdot k} \tag{6.1}$$

for $k\to 0$. These lepton propagators will be called "enhancers". Logarithmic IR divergence takes place when k-integration is carried out and the soft photon singularity is assisted by two enhancers. When the vertex Feynman diagram $\mathcal{G}(k)$ in question has a self-energy subdiagram, we find three enhancers due to the kinematical constraint of the two-point vertex, so that we find the IR divergence to be linear. The IR divergence becomes even more severe when the diagram $\mathcal{G}(k)$ has more than one self-energy subdiagram, which effectively brings in a number of two-point vertices.

To handle the IR divergences, we again adopt a subtractive approach, in which an integral of IR subtraction terms is constructed in such a way that it cancels out the IR divergence of the integral $M_{\mathcal{G}}^{(2n)}$ of Eq. (4.31) point-by-point in the Feynman parameter space.

6.2. *IR divergence caused by residual self-mass*

One type of IR divergence appears as a consequence of our particular treatment of the UV divergences by means of K-operation. Suppose a diagram $\mathcal{G}$ has a self-energy subdiagram $\mathcal{S}$. As is readily seen from the analysis of Feynman diagrams, this divergence is not the source of the real problem since it must be canceled exactly by the mass-renormalization counter term $\delta m_{\mathcal{S}}\, M_{\mathcal{G}/\mathcal{S}\,(i^\star)}$, where $\delta m_{\mathcal{S}}$ is the (UV-divergent) self-mass associated with the subdiagram $\mathcal{S}$ defined on the mass shell. The reduced magnetic moment amplitude $M_{\mathcal{G}/\mathcal{S}\,(i^\star)}$ is the one that has a linear IR divergence. As a consequence,

$$M_{\mathcal{G}}-\delta m_{\mathcal{S}}\, M_{\mathcal{G}/\mathcal{S}\,(i^\star)} \tag{6.2}$$

is free from linear IR divergence. Although this cancellation is analytically valid, however, it is not a point-wise cancellation in the domain of $M_{\mathcal{G}}$. Our problem is thus to translate the second term into a form that is defined in the same domain as that of $M_{\mathcal{G}}$ and cancels the IR divergence of $M_{\mathcal{G}}$ point-by-point.

Now, as was noted in Eq. (5.37), the K-operation for the subdiagram $\mathcal{S}$ acting on $M_{\mathcal{G}}$ creates

$$\mathsf{K}_{\mathcal{S}}M_{\mathcal{G}}=\delta m_{\mathcal{S}}^{\mathrm{UV}}\, M_{\mathcal{G}/\mathcal{S}\,(i^\star)}+B_{\mathcal{S}}^{\mathrm{UV}}\, M_{\mathcal{G}/[\mathcal{S},i']}. \tag{6.3}$$

If we find an integral that causes point-wise cancellation of the linear IR divergence in the domain of $M_{\mathcal{G}}$ and also produces factorization as

$$\widetilde{\delta m}_{\mathcal{S}}M_{\mathcal{G}/\mathcal{S}\,(i^\star)}, \tag{6.4}$$

where

$$\widetilde{\delta m}_{\mathcal{S}}\equiv\delta m_{\mathcal{S}}-\delta m_{\mathcal{S}}^{\mathrm{UV}}, \tag{6.5}$$

then from Eqs. (6.3) and (6.4) we would have

$$\mathsf{K}_{\mathcal{S}}M_{\mathcal{G}}+\widetilde{\delta m}_{\mathcal{S}}M_{\mathcal{G}/\mathcal{S}\,(i^\star)}=\delta m_{\mathcal{S}}\, M_{\mathcal{G}/\mathcal{S}\,(i^\star)}+B_{\mathcal{S}}^{\mathrm{UV}}\, M_{\mathcal{G}/[\mathcal{S},i']}. \tag{6.6}$$

If we schematically introduce an operator $\mathsf{R}_{\mathcal{S}}$ that produces the integral of Eq. (6.4) as

$$\mathsf{R}_{\mathcal{S}}M_{\mathcal{G}}\equiv\widetilde{\delta m}_{\mathcal{S}}M_{\mathcal{G}/\mathcal{S}\,(i^\star)}, \tag{6.7}$$

Eq. (6.6) would then be written as

$$(\mathsf{K}_{\mathcal{S}}+\mathsf{R}_{\mathcal{S}})M_{\mathcal{G}}=\delta m_{\mathcal{S}}\, M_{\mathcal{G}/\mathcal{S}\,(i^\star)}+B_{\mathcal{S}}^{\mathrm{UV}}\, M_{\mathcal{G}/[\mathcal{S},i']}. \tag{6.8}$$

It turns out that it is not difficult to construct such an integral if we use the factorization formula (5.34) backward. Furthermore, it can be readily incorporated in our automation algorithm. We call this subtraction scheme the residual self-mass subtraction, or "R-subtraction" operation.

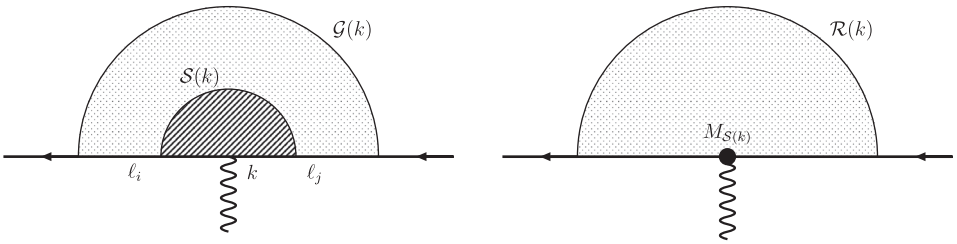

Fig. 10. A vertex diagram $\mathcal{G}(k)$ and a subdiagram $\mathcal{S}(k)$ (left), the reduced vertex diagram $\mathcal{R}(k)$ with a vertex $M_{\mathcal{S}(k)}$ (right). Reproduced with permission from [36].

6.3. I-subtraction operation

After the linear (or worse) IR divergences are disposed of by the K-operation and R-subtraction operation, we are still left with logarithmic IR divergences. To treat these divergences, let us consider a vertex diagram $\mathcal{G}(k)$ that has a subdiagram $\mathcal{S}(k)$. Here, k refers to an external photon vertex attached to a lepton line ℓ_k of the self-energy-like subdiagram $\mathcal{S}$. The reduced diagram $\mathcal{S}(k)$ is connected to the remaining part of $\mathcal{G}(k)$ by lepton lines ℓ_i and ℓ_j. (See Fig. 10 (left).) We denote the reduced diagram as $R(k) \equiv G(k)/S(k)$.

This diagram exhibits IR-divergent behavior when the momenta of (all or some) photons in $\mathcal{R}$ go to zero, accompanied by the enhancers ℓ_i and ℓ_j. The substructure $\mathcal{S}(k)$ to which these enhancers are attached can be considered as a magnetic moment of the lower order. Thus the amplitude in this limit becomes that of the diagram $\mathcal{R}(k)$, obtained by replacing $\mathcal{S}(k)$ by a vertex that is weighted by $M_{\mathcal{S}(k)}$, as shown in Fig. 10 (right). $\mathcal{R}(k)$ develops a logarithmic IR divergence, as is easily verified by power-counting.

Since we are dealing with the Ward–Takahashi-summed diagram defined by Eq. (4.30), we have to consider the sum of contributions of vertex diagrams $\mathcal{S}(k)$ which are obtained by inserting an external vertex k to the self-energy-like diagram $\mathcal{S}$ in every possible way. In the calculation of the diagram $\mathcal{G}$, the IR divergence associated with the substructure $\mathcal{S}$ has a form that consists of contributions from the vertex diagram $\mathcal{R}(k)$ and the magnetic projection of the diagram $\mathcal{S}$. The IR divergence is contained in the vertex renormalization constant $L_{\mathcal{R}(k)}$.

For the explicit expression of the IR subtraction term that cancels the divergence mentioned above, we consider the term

$$\widetilde{L}_{\mathcal{G}/\mathcal{S}(k)} M_{\mathcal{S}}, \tag{6.9}$$

where $\widetilde{L}$ is the residual part of the vertex renormalization constant

$$\widetilde{L}_{\mathcal{G}/\mathcal{S}(k)} \equiv L_{\mathcal{G}/\mathcal{S}(k)} - L^{\mathrm{UV}}_{\mathcal{G}/\mathcal{S}(k)}. \tag{6.10}$$

We construct an integral that corresponds to Eq. (6.9) in the domain of $M_{\mathcal{G}}$. We call this subtraction scheme the "I-subtraction" operation.

All quantities appearing in the IR subtraction terms, the magnetic moment parts $M_{\mathcal{G}}$ and $M_{\mathcal{G}(i^\star)}$, and part of the renormalization constants $\widetilde{\delta m}_{\mathcal{G}}$ and $\widetilde{L}_{\mathcal{G}}$, may contain UV subdivergences that have to be subtracted by K-operations. We then introduce the new notations L^{R} and δm^{R}, similar to M^{R} in

(5.38), for the UV-divergence-free quantities as

$$L^{\mathrm{R}}_{\mathcal{G}} = \sum_f \left[\prod_{\mathcal{S}_i \in f} (-\mathsf{K}_{\mathcal{S}}) \right] \widetilde{L_{\mathcal{G}}}, \tag{6.11}$$

$$\delta m^{\mathrm{R}}_{\mathcal{G}} = \sum_f \left[\prod_{\mathcal{S}_i \in f} (-\mathsf{K}_{\mathcal{S}}) \right] \widetilde{\delta m_{\mathcal{G}}}, \tag{6.12}$$

where the sum is taken over all forests f of a diagram $\mathcal{G}$.

Using the quantities with the superscript "R", we redefine R- and I-subtraction operations as follows:

$$\mathsf{R}_{\mathcal{S}} M_{\mathcal{G}} \equiv \delta m^{\mathrm{R}}_{\mathcal{S}}\, M^{\mathrm{R}}_{\mathcal{G}/\mathcal{S}\,(i^\star)}, \tag{6.13}$$

$$\mathsf{I}_{\mathcal{S}} M_{\mathcal{G}} \equiv L^{\mathrm{R}}_{\mathcal{S}}\, M^{\mathrm{R}}_{\mathcal{G}/\mathcal{S}}. \tag{6.14}$$

6.4. Nested IR singularity and annotated forests

A diagram may contain more than one source of IR divergences that lead to complicated divergence structure. They are treated by combinations of I- and R-subtraction operations conducted by *annotated forests*. For a diagram $\mathcal{G}$ containing a single self-energy subdiagram $\mathcal{S}$, the associated IR divergences are treated by these two types of operations, and the IR-finite amplitude is thus given by

$$\Delta M_{\mathcal{G}} = M^R_{\mathcal{G}} - \mathsf{I}_{\mathcal{S}} M^{\mathrm{R}}_{\mathcal{G}} - \mathsf{R}_{\mathcal{S}} M^{\mathrm{R}}_{\mathcal{G}}. \tag{6.15}$$

When the diagram has more than one such self-energy subdiagram, the IR divergences due to all those subdiagrams have to be subtracted. The finite amplitude free from both IR and UV divergences is obtained schematically by

$$\Delta M_{\mathcal{G}} = \prod_{\mathcal{S}} (1 - \mathsf{I}_{\mathcal{S}} - \mathsf{R}_{\mathcal{S}}) M^{\mathrm{R}}_{\mathcal{G}}, \tag{6.16}$$

where the product is taken over all self-energy subdiagrams of the diagram $\mathcal{G}$.

By expanding the product in Eq. (6.16), we are led to a forest-like structure that is analogous to the renormalization of UV divergences. In this case, a forest consists of only self-energy subdiagrams, and each subdiagram is assigned a distinction of R-subtraction or I-subtraction. We call such a forest an "annotated forest". Equation (6.16) is thus turned into a sum over all annotated forests $\tilde{f}$ as

$$\sum_{\tilde{f}} (-\mathsf{I}_{\mathcal{S}_i}) \cdots (-\mathsf{R}_{\mathcal{S}_j}) \cdots M^{\mathrm{R}}_{\mathcal{G}}, \tag{6.17}$$

where $\mathcal{S}_i, \ldots$ and $\mathcal{S}_j, \ldots$ are elements of the annotated forest $\tilde{f}$ that are assigned to I-subtraction operations and R-subtraction operations, respectively. Those operators act on the amplitude $M^{\mathrm{R}}_{\mathcal{G}}$ successively.

A forest is represented as a tree form that expresses the inclusion relation of the subdiagrams in the forest. (See Fig. 11.) We assign each subdiagram to a node. If a subdiagram is included in another subdiagram $\mathcal{S}$, it is expressed as a child node of the node assigned to $\mathcal{S}$. We consider the diagram $\mathcal{G}$ itself as the root node of the tree. For later convenience, we denote the subdiagrams that contain another subdiagram $\mathcal{S}$ as (direct) ancestors of $\mathcal{S}$, and the subdiagrams that are included in $\mathcal{S}$ as descendants of $\mathcal{S}$.

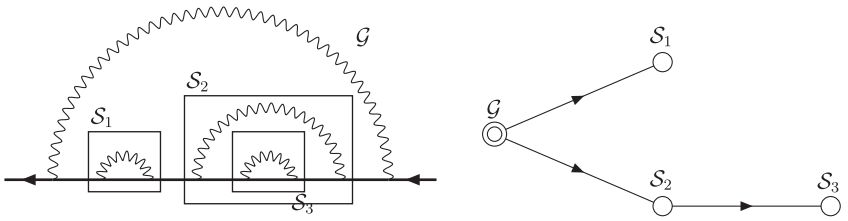

Fig. 11. An example of nested subdiagrams of a forest and the tree representation. Reproduced with permission from [36].

For the annotated forest, a distinct operation of I-subtraction or R-subtraction is assigned to the node. We call such a tree an *annotated tree* hereafter. Each node is then translated into the component term of the reduced diagram.

For the simplest example in which $\mathcal{G}$ has a single subdiagram $\mathcal{S}$, the tree form of the forest is shown as follows:

When we consider the $\mathsf{I}_{\mathcal{S}}$ operation, the result is given as a product of a vertex renormalization constant $L^{\mathrm{R}}_{\mathcal{R}(k)}$ for the part of the diagram $\mathcal{R}(k) \equiv \mathcal{G}/\mathcal{S}(k)$ and a magnetic moment part $M^{\mathrm{R}}_{\mathcal{S}}$ for the subdiagram $\mathcal{S}$. These subdiagram parts are related to the nodes in the above tree labeled by $\mathcal{G}$ and $\mathcal{S}$, respectively. Thus we represent the assignment of components of the subtraction term graphically as follows:

When the R-subtraction $\mathsf{R}_{\mathcal{S}}$ is considered, the assignment is represented in a similar manner, as follows:

Here, the subdiagram $\mathcal{S}$ corresponding to the right node is related to the residual self-mass term $\delta m^{\mathrm{R}}_{\mathcal{S}}$, and the reduced diagram $\mathcal{G}/\mathcal{S}$ $(i^\star)$ that corresponds to the left node is assigned to the magnetic moment part $M^{\mathrm{R}}_{\mathcal{G}/\mathcal{S}\,(i^\star)}$.

This representation can be extended to more general cases. For an annotated forest that corresponds to a nested singularity, the successive operations of I-/R-subtractions in an appropriate order are interpreted to extend the tree by following the relevant process shown above. Then we obtain a tree representation of the annotated forest in which distinct types of M^{R}-, L^{R}-, or δm^{R} are assigned to the nodes.

The nodes of the tree are related to the reduced diagrams, and so the annotated tree has a direct interpretation of the IR subtraction term in the form of a product of the component terms for their respective reduced diagrams. Since the tree expresses the nested structure of subdiagrams in the forest, the relevant set of Feynman parameters for the component term, i.e., how the reduced subdiagram for the component term is embedded in the original diagram, can be easily read off from the tree. This feature is crucial in constructing the IR subtraction integral so that the point-wise subtraction of IR singularities is achieved.

Thus far, the annotated tree provides a graphical representation of the annotated forest, and it has a one-to-one correspondence. It is readily translated into a symbolic form of the associated IR subtraction term, which is also significant for the residual renormalization step. The set of IR subtraction

terms can be obtained by finding the set of annotated trees that have proper assignment of types to the tree nodes consisting of self-energy subdiagrams.

They are summarized as follows:

1. There is one and only one node to which the magnetic moment part M^{R} is assigned.
2. The nodes that are assigned to the I-subtraction, L^{R}, are restricted to the ancestor nodes of the magnetic moment part.
3. The nodes that are assigned to the residual self-mass subtraction, δm^{R}, do not appear as ancestor nodes of the magnetic moment part.

It turns out that to satisfy these rules the assignment is uniquely determined once a node is chosen for the magnetic moment part. We first pick up a node that is assigned to the magnetic part M^{R}, and then the nodes that lie as ancestors of the M-node are associated with the I-subtractions. The remaining nodes are assigned to the R-subtractions.

We have finally obtained the finite magnetic moment amplitude $\Delta M_{\mathcal{G}}$ by applying the R- and I-subtractions following the annotated forest formula:

$$\Delta M_{\mathcal{G}} = \sum_{\tilde{f}} (-\mathsf{I}_{\mathcal{S}_i}) \times \cdots (-\mathsf{R}_{\mathcal{S}_j}) \times \cdots M^{\mathrm{R}}_{\mathcal{G}}, \tag{6.18}$$

where the sum is over all annotated forests $\tilde{f}$ constructed for the diagram $\mathcal{G}$. $\Delta M_{\mathcal{G}}$ is numerically evaluated by the adaptive-iterative Monte Carlo integration program VEGAS [93].

7. Residual renormalization: Examples of diagrams without a fermion loop

The construction of UV- and IR-finite integrals $\Delta M_{\mathcal{G}}$ for the gauge-invariant set is outlined in the preceding sections. To relate them to the standard on-shell renormalization, however, we have to perform another step, which we call *residual renormalization*. The derivation of the residual renormalization formula relies only on graphical information, so that it does not require the explicit form of $\Delta M_{\mathcal{G}}$.

For the gauge-invariant set of diagrams without a fermion loop, hereafter called q-type, once finite integrals and residual renormalization formulae are constructed, we are ready to calculate their $g-2$ contribution. Residual renormalization formulae for diagrams with vacuum-polarization subdiagrams can be readily derived from the q-type formulae. Diagrams with an l-l loop can be formulated by a slight modification of the method adopted for the q-type diagrams.

Because of shortage of space, we present here only examples of residual renormalization for the cases of the second, fourth, and sixth orders. A detailed description of residual renormalization for q-type diagrams up to the eighth order is given in Ref. [46]. Formulae for the 10th-order case are presented in T. Aoyama et al. (manuscript in preparation).

7.1. Second order

The second-order calculation is easy even if we use the vertex diagram directly. But, for higher-order calculations, we need the second-order amplitude in the form summed using the Ward–Takahashi identity, which is

$$a^{(2)} = \Delta M_2 = M_2 = \left(\frac{-1}{4}\right) \int_0^1 dz_1 \frac{N_0 + Z_0}{U^2 V}, \tag{7.1}$$

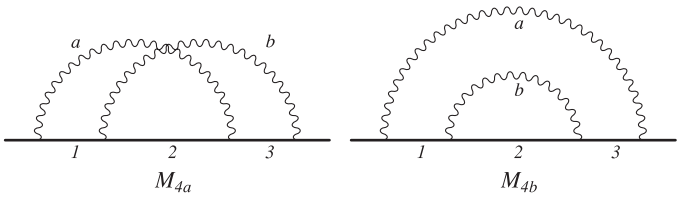

Fig. 12. Fourth-order self-energy-like diagrams without a fermion loop. The crossing and rainbow diagrams are called M_{4a} and M_{4b}. The Feynman parameters z_1, z_2, z_3 and z_a, z_b are assigned to the fermion lines and photon lines, respectively, as shown in the figures. Reproduced with permission from [43].

where the Feynman parameters assigned to the electron and photon lines are z_1 and z_a, respectively, and

$$V = z_1 - G, \quad U = z_1 + z_a = 1, \quad G = z_1 A_1, \quad A_1 = 1 - z_1/U,$$
$$N_0 = 4G(A_1 - 2), \quad Z_0 = 4z_1 A_1. \tag{7.2}$$

This is a finite integral and neither UV nor IR subtractions are needed. Hence, no residual renormalization is required in this case.

7.2. Fourth-order q-type diagrams

There are two diagrams of the fourth-order q-type, as shown in Fig. 12. Let us begin with the consideration of the standard on-shell renormalization of the fourth-order magnetic moment $a^{(4)}[q\text{-type}]$, which can be expressed in the form

$$a^{(4)}[q\text{-type}] = M_{4a} + M_{4b} - 2L_2 M_2 - B_2 M_2 - \delta m_2 M_{2^*}, \tag{7.3}$$

where M_2 is the second-order magnetic moment and M_{2^*} is obtained from M_2 by inserting a two-point vertex in the lepton line of M_2. L_2, B_2, and δm_2 are the second-order vertex-, wavefunction-, and mass-renormalization constants, respectively, determined with the standard on-shell condition.

The UV subtraction terms of the self-energy-like diagram M_{4a} are listed as

forests	K-operation	subtraction term
$\{1, 2; a\}$	K_{12}	$L_2^{\mathrm{UV}} M_2$
$\{2, 3; b\}$	K_{23}	$L_2^{\mathrm{UV}} M_2$,

(7.4)

where the subdiagrams are expressed by their line indices enclosed by braces, and the subscripts of K-operations distinguish the subdiagram by the indices of their fermion lines. Note that no IR subtraction is needed because M_{4a} has no self-energy subdiagram.

The amplitude M_{4a} is given by the Feynman parametric integral

$$M_{4a} = \left(-\frac{1}{4}\right)^2 2 \int \frac{(dz)_{\mathcal{G}}}{U^2} \left[\frac{E_0 + C_0}{V} + \frac{N_0 + Z_0}{V^2} + \frac{N_1 + Z_1}{UV}\right], \tag{7.5}$$

where the *building blocks* are

$$(dz)_{\mathcal{G}} = dz_1 dz_2 dz_3 dz_a dz_b \delta(1 - z_1 - z_2 - z_3 - z_a - z_b),$$
$$U = z_2(z_{1a} + z_{3b}) + z_{1a} z_{3b}, \quad B_{12} = z_{3b}, \quad B_{23} = z_{1a}, \quad B_{13} = -z_2,$$
$$B_{11} = z_{3b} + z_2, \quad B_{22} = z_{1a} + z_{3b}, \quad B_{33} = z_{1a} + z_2,$$
$$V = z_{123} - G, \quad G = z_1 A_1 + z_2 A_2 + z_2 A_3,$$
$$A_i = 1 - (z_1 B_{1i} + z_2 B_{2i} + z_3 B_{3i})/U, \quad i = 1, 2, 3. \tag{7.6}$$

The integrand of M_{4a} is given by

$$\begin{aligned}
E_0 &= 8(2A_1A_2A_3 - A_1A_2 - A_2A_3 - A_3A_1),\\
C_0 &= -8(C_{12} + C_{13} + C_{23}),\\
N_0 &= 8G(2A_1A_2A_3 - A_1A_2 - A_2A_3 - A_3A_1 - A_1 - A_2 - A_3),\\
Z_0 &= 8z_1(-A_1 + A_2 + A_3 + A_1A_2 + A_1A_3 - A_2A_3)\\
&\quad + 8z_2(-A_1 + A_2 - A_3 - A_1A_2 + A_1A_3 - A_2A_3 + 2A_1A_2A_3)\\
&\quad + 8z_3(A_1 + A_2 - A_3 - A_1A_2 + A_1A_3 + A_2A_3),\\
N_1 &= 8G[2(B_{12} + B_{23} + B_{13}) - A_1B_{23} - 4A_2B_{13} - A_3B_{12}],\\
Z_1 &= 8z_1(-A_1B_{23} + A_3B_{12} - B_{12} - B_{13})\\
&\quad + 8z_2(-A_1B_{23} - 4A_2B_{13} - A_3B_{12} + B_{12} + B_{23})\\
&\quad + 8z_3(A_1B_{23} - A_3B_{12} - B_{23} - B_{13}).
\end{aligned} \tag{7.7}$$

The finite amplitude is then defined as

$$\Delta M_{4a} \equiv (1 - \mathsf{K}_{12} - \mathsf{K}_{23})M_{4a} = M_{4a} - 2L_2^{\mathrm{UV}}M_2. \tag{7.8}$$

The second term of (7.8) is used for computer programing of ΔM_{4a}, while the third term is used to derive the residual renormalization formula. The finite integral ΔM_{4a} is ready to be numerically evaluated by VEGAS.

We give the explicit form of $\mathsf{K}_{12}M_{4a}$ as an example of the K-operation. The form of the integrand obtained by the K_{12} operation is

$$N_1 = 8GB_{12}(2 - A_3), \quad Z_1 = -8z_3A_3B_{12}, \quad N_0 = C_0 = E_0 = Z_0 = 0, \tag{7.9}$$

where the building blocks are those obtained by the K_{12}-operation

$$\begin{gathered}
U = z_{12a}z_{3b}, \quad B_{13} = B_{23} = 0, \quad B_{33} = z_{12a}, \quad B_{11} = B_{12} = B_{22} = z_{3b},\\
V = z_{123} - G, \quad G = z_1A_1 + z_2A_2 + z_3A_3,\\
A_i = 1 - z_1B_{1i} - z_2B_{2i} - z_3B_{3i}, \quad i = 1, 2, 3.
\end{gathered} \tag{7.10}$$

$\mathsf{K}_{23}M_{4a}$ can be constructed in a similar way.

The rainbow diagram M_{4b} has both UV and IR divergences. The UV divergence arises from the self-energy subdiagram $\{2; b\}$ and can be handled by the K_2-operation:

forests	K-operation	subtraction term
$\{2; b\}$	K_2	$B_2^{\mathrm{UV}}M_2 + \delta m_2 M_{2^\star}$

. (7.11)

Then the UV-finite amplitude is given by

$$M_{4b}^{\mathrm{R}} = (1 - \mathsf{K}_2)M_{4b} = M_{4b} - (B_2^{\mathrm{UV}}M_2 + \delta m_2 M_{2^*}). \tag{7.12}$$

The IR divergences occur when the loop momentum of the photon a vanishes. In this limit, the self-energy subdiagram $\{2; b\}$ behaves as a second-order magnetic moment M_2 and can be replaced by a point vertex. The residual diagram $\{1, 3; a\}$ then resembles the second-order vertex diagram.

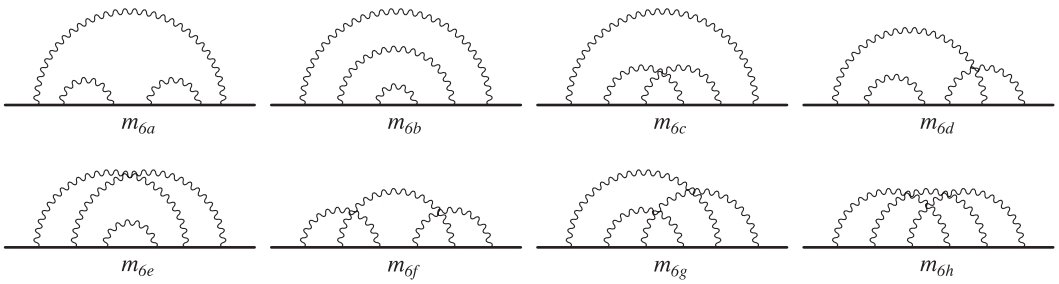

Fig. 13. Sixth-order self-energy-like diagrams without a fermion loop. They represents 50 vertex diagrams in total. Reproduced with permission from [45].

From this observation, the IR divergence of M_{4b}^{R} can be subtracted by performing an I_{13}-subtraction operation:

$$\begin{array}{lll} \text{annotated forests} & R\text{- and/or } I\text{-subtractions} & \text{subtraction term} \\ \{2;b\} & \mathsf{I}_{13} & L_2^{\mathrm{R}} M_2 \end{array} . \tag{7.13}$$

The finite amplitude is then obtained as

$$\Delta M_{4b} = (1 - \mathsf{I}_{13}) M_{4b}^{\mathrm{R}} = M_{4b}^{\mathrm{R}} - L_2^{\mathrm{R}} M_2. \tag{7.14}$$

The second term will be expressed in the same Feynman parameter space of M_{4b} so that a point-wise subtraction should be realized. The finite amplitude ΔM_{4b} is to be numerically evaluated by VEGAS.

The second-order renormalization constants L_2 and B_2 are decomposed such that

$$L_2 = L_2^{\mathrm{UV}} + L_2^{\mathrm{R}}, \quad B_2 = B_2^{\mathrm{UV}} + B_2^{\mathrm{R}}, \quad \Delta L B_2 \equiv L_2^{\mathrm{R}} + B_2^{\mathrm{R}}. \tag{7.15}$$

Because of the Ward–Takahashi identity $L_2 + B_2 = 0$, the IR divergence in L_2^{R} and B_2^{R} cancels out and the sum $\Delta L B_2$ is finite.

Substituting (7.8), (7.12), (7.14), and (7.15) into (7.3), we obtain the expression written down with *finite quantities only*:

$$a^{(4)}[q\text{-type}] = \Delta M_{4a} + \Delta M_{4b} - \Delta L B_2 M_2, \tag{7.16}$$

where the last term $-\Delta L B_2 M_2$ is the residual renormalization term. Substituting the numerical values

$$\Delta M_{4a} = 0.218\,347\,(32), \quad \Delta M_{4b} = -0.187\,478\,(35), \quad \Delta L B_2 = 0.75, \quad M_2 = 0.5 \tag{7.17}$$

into the residual renormalization formula (7.16), we obtain

$$a^{(4)}[q\text{-type}] = -0.344\,131\,(48), \tag{7.18}$$

which is consistent with the analytic result $a^{(4)}[q\text{-type}] = -0.344\,166\cdots$ [23,24].

7.3. Sixth-order q-type diagrams

The sixth-order q-type diagram is evaluated in a way similar to the fourth-order q-type. R-subtraction appears for the first time in this order for the diagrams m_{6b} and m_{6c} shown in Fig. 13, both of which contain a fourth-order self-energy subdiagram.

As an example, let us explain the construction of the finite amplitude of the diagram m_{6c}. The fermion lines are labeled $1, 2, \ldots, 5$ from left to right, and the photon lines are labeled a, b, c.

The UV-divergent subdiagrams of m_{6c} are $\{2,3,4;b,c\}$, $\{2,3;b\}$, and $\{3,4;c\}$. Five UV forests constructed from them and their corresponding K-operations are

forests	K-operation	subtraction terms
$\{2,3,4;b,c\}$	K_{234}	$B_{4a}^{\rm UV}M_2+\delta m_{4a}^{\rm UV}M_{2^*}$
$\{2,3;b,c\}$	K_{23}	$L_2^{\rm UV}M_{4b}$
$\{3,4;c\}$	K_{34}	$L_2^{\rm UV}M_{4b}$
$\{2,3,4;b,c\}\{2,3;b\}$	$\mathsf{K}_{234}\mathsf{K}_{23}$	$L_2^{\rm UV}(B_2^{\rm UV}M_2+\delta m_2 M_{2^*})$
$\{2,3,4;b,c\}\{3,4;c\}$	$\mathsf{K}_{234}\mathsf{K}_{34}$	$L_2^{\rm UV}(B_2^{\rm UV}M_2+\delta m_2 M_{2^*})$

The self-energy subdiagram in m_{6c} is {2,3,4;b,c} only. The IR annotated forests are constructed as

annotated forests	$R-$ or I-subtraction	subtraction terms
$\{2,3,4;b,c\}$	R_{234}	$\delta m_{4a}^{\rm R}M_{2^*}$
$\{2,3,4;b,c\}$	I_{15}	$L_2^{\rm R}M_{4a}^{\rm R}$

Note that $M_{4a}^{\rm R}=\Delta M_{4a}$ given in (7.8), because no IR divergence is found in M_{4a}.

The finite amplitude is then obtained from

$$\Delta M_{6c}=(1-\mathsf{K}_{234}-\mathsf{K}_{23}-\mathsf{K}_{34}+\mathsf{K}_{234}\mathsf{K}_{23}+\mathsf{K}_{234}\mathsf{K}_{34}-\mathsf{R}_{234}-\mathsf{I}_{15})M_{6c}. \tag{7.19}$$

Adding up all self-energy-like diagrams of Fig. 13, we obtain the final form of $a_e^{(6)}[q\text{-type}]$ as the sum of finite quantities only:

$$a_e^{(6)}[q\text{-type}]=\Delta M_6-3\Delta M_4\Delta LB_2+\Delta M_2\{-\Delta LB_4+2(\Delta LB_2)^2\}, \tag{7.20}$$

where the last three terms are residual renormalization terms, and

$$\Delta M_6=\sum_{i=a,\cdots h}\eta_i\Delta M_{6i},\quad \eta_i=\begin{cases}2 & \text{for } i=d,g,\\ 1 & \text{otherwise,}\end{cases} \tag{7.21}$$

$$\Delta LB_4=\sum_{i=a,b}\left(B_{4i}^{\rm R}+\sum_{j=1,2,3}L_{4i(j)}^{\rm R}\right)-L_2^{\rm R}\Delta LB_2. \tag{7.22}$$

B_{4i} and $L_{4i(j)}$ are the wavefunction- and vertex-renormalization constants derived from the self-energy diagram M_{4i} in Fig. 12.

Acknowledgements

This work is supported in part by the JSPS Grant-in-Aid for Scientific Research (C) 20540261 and (C) 23540331. T.K.'s work is supported in part by the US National Science Foundation under Grant No. NSF-PHY-0757868. Numerical calculations were conducted on the RIKEN Supercombined Cluster System (RSCC) and the RIKEN Integrated Cluster of Clusters (RICC) supercomputing systems.

References

[1] P. Kusch and H. M. Foley, Phys. Rev. **72**, 1256 (1947).
[2] P. Kusch and H. M. Foley, Phys. Rev. **73**, 412 (1948).
[3] P. Kusch and H. M. Foley, Phys. Rev. **74**, 250 (1948).
[4] W. E. Lamb and R. C. Retherford, Phys. Rev. **72**, 241 (1947).
[5] S. Tomonaga, Prog. Theor. Phys. **1**, 27 (1946).
[6] S. Tomonaga, Phys. Rev. **74**, 224 (1948).
[7] J. S. Schwinger, Phys. Rev. **74**, 1439 (1948).
[8] J. S. Schwinger, Phys. Rev. **73**, 416L (1948); **75**, 898 (1949) [erratum].

[9] B. Lee Roberts and W. J. Marciano, *Lepton Dipole Moments* (World Scientific, Singapore, 2010).
[10] B. Odom, D. Hanneke, B. D'Urso, and G. Gabrielse, Phys. Rev. Lett. **97**, 030801 (2006).
[11] D. Hanneke, S. Fogwell, and G. Gabrielse, Phys. Rev. Lett. **100**, 120801 (2008).
[12] D. Hanneke, S. Fogwell Hoogerheide, and G. Gabrielse, Phys. Rev. A **83**, 052122 (2011).
[13] R. S. Van Dyck, P. B. Schwinberg, and H. G. Dehmelt, Phys. Rev. Lett. **59**, 26 (1987).
[14] G. W. Bennett et al. [Muon g−2 Collaboration], Phys. Rev. Lett. **92**, 161802 (2004).
[15] G. W. Bennett et al. [Muon g−2 Collaboration], Phys. Rev. D **73**, 072003 (2006).
[16] P. J. Mohr, B. N. Taylor, and D. B. Newell, Rev. Mod. Phys. **80**, 633 (2008).
[17] B. Lee Roberts, Chinese Phys. C **34**, 741 (2010).
[18] C. Amsler et al. [Particle Data Group], Phys. Lett. B **667**, 1 (2008).
[19] B. Lee Roberts [Fermilab P989 Collaboration], Nucl. Phys. Proc. Suppl. **218**, 237 (2011).
[20] T. Mibe [J-PARC g−2/EDM Collaboration], Nucl. Phys. Proc. Suppl. **218**, 242 (2011).
[21] H. Iinuma [J-PARC g−2/EDM Collaboration], J. Phys.: Conf. Ser. **295**, 012032 (2011).
[22] P. J. Mohr, B. N. Taylor, and D. B. Newell, arXiv:1203.5425.
[23] A. Petermann, Helv. Phys. Acta **30**, 407 (1957).
[24] C. M. Sommerfield, Phys. Rev. **107**, 328 (1957).
[25] S. Laporta and E. Remiddi, Phys. Lett. B **379**, 283 (1996).
[26] H. H. Elend, Phys. Lett. **20**, 682 (1966); **21**, 720 (1966) [erratum].
[27] M. A. Samuel and G. Li, Phys. Rev. D **44**, 3935 (1991); **48**, 1879 (1993) [erratum].
[28] G. Li, R. Mendel and M. A. Samuel, Phys. Rev. D **47**, 1723 (1993).
[29] S. Laporta, Nuovo Cim. A **106**, 675 (1993).
[30] S. Laporta and E. Remiddi, Phys. Lett. B **301**, 440 (1993).
[31] T. Kinoshita, Phys. Rev. Lett. **75**, 4728 (1995).
[32] T. Kinoshita and M. Nio, Phys. Rev. Lett. **90**, 021803 (2003).
[33] T. Kinoshita and M. Nio, Phys. Rev. D **73**, 013003 (2006).
[34] T. Kinoshita and M. Nio, Phys. Rev. D **73**, 053007 (2006).
[35] T. Aoyama, M. Hayakawa, T. Kinoshita, and M. Nio, Nucl. Phys. B **740**, 138 (2006).
[36] T. Aoyama, M. Hayakawa, T. Kinoshita, and M. Nio, Nucl. Phys. B **796**, 184 (2008).
[37] T. Aoyama, M. Hayakawa, T. Kinoshita, and M. Nio, Phys. Rev. Lett. **99**, 110406 (2007).
[38] T. Aoyama, M. Hayakawa, T. Kinoshita, and M. Nio, Phys. Rev. D **77**, 053012 (2008).
[39] T. Aoyama, M. Hayakawa, T. Kinoshita, M. Nio, and N. Watanabe, Phys. Rev. D **78**, 053005 (2008).
[40] T. Aoyama, M. Hayakawa, T. Kinoshita, and M. Nio, Phys. Rev. D **78**, 113006 (2008).
[41] T. Aoyama, K. Asano, M. Hayakawa, T. Kinoshita, M. Nio, and N. Watanabe, Phys. Rev. D **81**, 053009 (2010).
[42] T. Aoyama, M. Hayakawa, T. Kinoshita, and M. Nio, Phys. Rev. D **82**, 113004 (2010).
[43] T. Aoyama, M. Hayakawa, T. Kinoshita, and M. Nio, Phys. Rev. D **83**, 053002 (2011).
[44] T. Aoyama, M. Hayakawa, T. Kinoshita, and M. Nio, Phys. Rev. D **83**, 053003 (2011).
[45] T. Aoyama, M. Hayakawa, T. Kinoshita, and M. Nio, Phys. Rev. D **84**, 053003 (2011).
[46] T. Aoyama, M. Hayakawa, T. Kinoshita, and M. Nio, Phys. Rev. D **85**, 033007 (2012).
[47] T. Aoyama, M. Hayakawa, T. Kinoshita, and M. Nio, Phys. Rev. D **85**, 093013 (2012).
[48] T. Aoyama, M. Hayakawa, T. Kinoshita, and M. Nio, Phys. Rev. Lett. **109**, 111807 (2012).
[49] M. Caffo, S. Turrini, and E. Remiddi, Nucl. Phys. B **141**, 302 (1978).
[50] S. Laporta, Phys. Lett. B **328**, 522 (1994).
[51] P. J. Mohr and B. N. Taylor, Rev. Mod. Phys. **72**, 351 (2000).
[52] D. Nomura and T. Teubner, arXiv:1208.4194(hep-ph).
[53] K. Hagiwara, R. Liao, A. D. Martin, D. Nomura, and T. Teubner, J. Phys. G: Nucl. Part. Phys. **38**, 085003 (2011).
[54] F. Jegerlehner and R. Szafron, Eur. Phys. J. C **71**, 1632 (2011).
[55] M. Davier, A. Hoecker, B. Malaescu, and Z. Zhang, Eur. Phys. J. C **71**, 1515 (2011).
[56] J. Prades, E. de Rafael, and A. Vainshtein, in "Lepton Dipole Momnets" edited by B. L. Roberts and W. J. Marciano (World Scientfic, Singapore, 2009) pp. 303–319.
[57] K. Fujikawa, B. W. Lee, and A. I. Sanda, Phys. Rev. D **6**, 2923 (1972).
[58] A. Czarnecki, B. Krause, and W. J. Marciano, Phys. Rev. Lett. **76**, 3267 (1996).
[59] M. Knecht, S. Peris, M. Perrottet, and E. De Rafael, J. High Energy Phys. **11**, 003 (2002).
[60] A. Czarnecki, W. J. Marciano, and A. Vainshtein, Phys. Rev. D **67**, 073006 (2003); **73**, 119901(E) (2006) [erratum].

[61] R. Bouchendira, P. Clade, S. Guellati-Khelifa, F. Nez, and F. Biraben, Phys. Rev. Lett. **106**, 080801 (2011).
[62] S. J. Brodsky and T. Kinoshita, Phys. Rev. D **3**, 356 (1971).
[63] T. Kinoshita, H. Kawai, and Y. Okamoto, Phys. Lett. B **254**, 235 (1991).
[64] H. Kawai, T. Kinoshita, and Y. Okamoto, Phys. Lett. B **260**, 193 (1991).
[65] A. L. Kataev, Phys. Rev. B **284**, 401 (1992).
[66] D. J. Broadhurst, A. L. Kataev, and O. V. Tarasov, Phys. Rev. B **298**, 445 (1993).
[67] A. L. Kataev and V. V. Starshenko, Phys. Rev. D **52**, 402 (1995).
[68] A. L. Kataev, Phys. Rev. D **74**, 073011 (2006).
[69] J. Aldins, T. Kinoshita, S. J. Brodsky, and A. J. Dufner, Phys. Rev. Lett. **23**, 441 (1969).
[70] J. Aldins, T. Kinoshita, S. J. Brodsky, and A. J. Dufner, Phys. Rev. D **1**, 2378 (1970).
[71] A. S. Elikhovskii, Yad. Fiz. **49**, 1056 (1989) [Sov. J. Phys. **49**, 654 (1989)].
[72] S. G. Karshenboim, Yad. Fiz. **56**, 252 (1993) [Phys. At. Nucl. **56**, 857 (1993)].
[73] M. A. Samuel and G. Li, Phys. Rev. D **44**, 3935 (1991).
[74] M. Passera, Phys. Rev. D **75**, 013002 (2007).
[75] A. Czarnecki and M. Skrzypek, Phys. Lett. B **449**, 354 (1999).
[76] T. Kinoshita and M. Nio, Phys. Rev. D **73**, 053007 (2006).
[77] T. Aoyama, M. Hayakawa, T. Kinoshita, and M. Nio, Phys. Rev. Lett. **109**, 111808 (2012).
[78] S. Laporta, Phys. Lett. B **312**, 495 (1993).
[79] J.-P. Aguilar, E. De Rafael, and D. Greynat, Phys. Rev. D **77**, 093010 (2008).
[80] B. Krause, Phys. Lett. B **390**, 392 (1997).
[81] F. Jegerlehner and A. Nyffeler, Phys. Rep. **477**, 1 (2009).
[82] K. Melnikov and A. Vainshtein, Phys. Rev. D **70**, 113006 (2004).
[83] J. Bijnens and J. Prades, Mod. Phys. Lett. A **22**, 767 (2007).
[84] J. Prades, E. de Rafael, and A. Vainshtein, in *Lepton Dipole Moments*, eds. B. Lee Roberts and W. J. Marciano (World Scientific, Singapore, 2009), pp. 303–319.
[85] A. Nyffeler, Phys. Rev. D **79**, 073012 (2009).
[86] P. Cvitanovic and T. Kinoshita, Phys. Rev. D **10**, 3978 (1974).
[87] T. Kinoshita, in *Quantum Electrodynamics*, ed. T. Kinoshita (World Scientific, Singapore, 1990), pp. 218–321.
[88] R. Karplus and N. M. Kroll, Phys. Rev. **77**, 536 (1950).
[89] P. Cvitanovic and T. Kinoshita, Phys. Rev. D **10**, 4007 (1974).
[90] P. Cvitanovic and T. Kinoshita, Phys. Rev. D **10**, 3991 (1974).
[91] N. Nakanishi, *Graph Theory and Feynman Integrals* (Gordon and Breach, New York, 1971).
[92] W. Zimmermann, Commun. Math. Phys. **15**, 208 (1969).
[93] G. P. Lepage, J. Comput. Phys. **27**, 192 (1978).